Nanoscale Advances

ROYAL SOCIETY OF CHEMISTRY

PAPER

View Article Online
View Journal | View Issue

Open Access Article. Published on 18 July 2025. Downloaded on 1/16/2026 6:16:01 PM.
This article is licensed under a Creative Commons Attribution-NonCommercial 3.0 Unported Licence.

Check for updates

Cite this: *Nanoscale Adv.*, 2025, **7**, 5561

# A multi-functional novel Z-scheme $ZnIn_2S_4$/g-$C_3N_5$ heterojunction catalyst for enhanced visible light active photocatalysis and antimicrobial action

Pratyush Kumar Sahu,[a] Aslisha Champati,[a] Alaka Rath,[a] Sovanika Pradhan,[ab] Abanti Pradhan[a] and Brundabana Naik *[a]

Photocatalysis represents a sustainable approach for cleaner energy production, wastewater treatment, and antimicrobial disinfection. Creating effective photocatalysts that respond to visible light is crucial for tackling worldwide challenges related to energy and the environment. Here, for the first time, we have reported a facile solvothermal strategy for the *in situ* growth of $ZnIn_2S_4$ nanoflowers on g-$C_3N_5$ nanoflakes, where the latter were synthesized *via* thermal polymerization followed by ultrasonic exfoliation. The resulting $ZnIn_2S_4$/g-$C_3N_5$ (ZCN-10) composite demonstrated outstanding photocatalytic activity, achieving 88.4% degradation of ciprofloxacin within 90 minutes under solar irradiation and producing 3368 μM $L^{-1}$ of $H_2O_2$ under visible light. This enhanced performance when compared to pristine $ZnIn_2S_4$ and g-$C_3N_5$ is attributed to the formation of a direct Z-scheme heterojunction, which promotes efficient charge separation, broadens light absorption, and optimizes the band structure and morphology. The ZCN-10 catalyst maintained high photocatalytic efficiency over four consecutive cycles and also exhibited notable antimicrobial activity, producing a 17 mm inhibition zone against *B. subtilis* and 30 mm inhibition zone against *E. coli*. Comprehensive analytical characterization confirmed the successful synthesis and structural integrity of the nanocomposite. Mechanistic studies, including radical scavenging and band structure analysis, revealed that the direct Z-scheme configuration significantly enhances charge carrier separation and utilization, facilitating the generation of reactive species such as superoxide ($^{\bullet}O_2^-$) and hydroxyl ($^{\bullet}OH$) radicals, which drive advanced oxidation processes (AOPs). This work highlights a promising route for developing earth-abundant, eco-friendly photocatalysts for environmental remediation and sustainable energy applications.

Received 30th May 2025
Accepted 17th July 2025

DOI: 10.1039/d5na00530b

rsc.li/nanoscale-advances

## 1. Introduction

The stark reality of environmental degradation casts a long shadow over our future. With 85% of global wetlands decimated and a staggering number of individuals lacking access to potable water and adequate sanitation, the planet's ecological health teeters precariously.[1] Adding to this already critical situation is the escalating threat posed by emerging contaminants, which not only intensify the strain on our limited freshwater resources but also introduce significant risks to ecology.[2–4] The persistent and escalating presence of antibiotics in aquatic environments has become a widely addressed environmental concern. Studies consistently reveal increasing antibiotic concentrations across diverse water systems, including surface water, groundwater, and sewage treatment plant effluents, highlighting a problem of significant and growing magnitude.[5,6] Specifically, the detection of ciprofloxacin (CIP), a quinolone antibiotic, raises serious concerns regarding its potential contribution to the proliferation of antibiotic resistance. The risks to both aquatic contribution ecosystems and human health are heightened by CIP's ability to facilitate the dissemination of antibiotic resistance genes (ARGs) within aquatic habitats. Furthermore, the limited effectiveness of current wastewater treatment methods in removing CIP compounds the problem of antibiotic contamination in water resources.[7] Conventional wastewater treatment approaches, both physiochemical and biological methodologies, have proven inadequate in addressing the challenge posed by CIP due to its substantial molecular weight and broad-spectrum antibacterial activity. In response, advanced oxidation processes (AOPs) have emerged as a promising remediation strategy for contaminated water. These processes leverage highly reactive radicals, such as hydroxyl ($^{\bullet}OH$) and superoxide ($^{\bullet}O_2^-$), to effectively degrade diverse inorganic–organic effluents.[8] Among the AOPs-including photocatalysis, electrochemical processes, Fenton reactions, non-thermal plasmas, ozonation, and sonolysis, photocatalysis garnered significant

[a]*Department of Chemistry, ITER, Siksha 'O' Anusandhan, Deemed to be University, Bhubaneswar, Odisha, India. E-mail: brundabananaik@soa.ac.in*

[b]*CSIR-Institute of Materials and Minerals Technology, Bhubaneswar, Odisha, India*

© 2025 The Author(s). Published by the Royal Society of Chemistry

Open Access Article. Published on 18 July 2025. Downloaded on 1/16/2026 6:16:01 PM. This article is licensed under a Creative Commons Attribution-NonCommercial 3.0 Unported Licence.

attention for its high efficiency, environmental sustainability, and reliance on renewable energy sources.[9–11]

Despite its advantages, photodegradation suffers from limited temporal efficiency, primarily due to its moderate response characteristics. Alternatively, the Fenton reaction offers an effective approach for antibiotic removal, employing hydrogen peroxide ($H_2O_2$) to generate potent oxidizing free radicals that facilitate rapid antibiotic breakdown and elimination. Beyond Fenton-mediated decomposition, $H_2O_2$ itself, recognized as a powerful and environmentally benign oxidant, finds application in diverse areas, including environmental remediation, pulp bleaching, and disinfection.[12] While these remediation techniques offer promise, they often require a continuous supply of $H_2O_2$, resulting in substantial treatment costs. Furthermore, the large-scale implementation of $H_2O_2$ production *via* traditional anthraquinone oxidation or electrocatalytic oxygen reduction is hampered by complexities, inherent safety risks, potential contamination, and elevated expenses.[13] Conversely, photocatalytic methods, which directly utilize solar energy to reduce oxygen, present a cost-effective alternative for $H_2O_2$ generation.[8] Therefore, the integration of simultaneous $H_2O_2$ production and photodegradation offers a potentially efficient strategy for the effective removal of antibiotics.[14,15] Apart from their well-known photocatalytic applications, nanomaterials play a crucial role in antimicrobial disinfection due to their unique physicochemical properties at the nanoscale.[16,17] Their extremely small size and high surface-to-volume ratio enable enhanced interaction with microbial cells, facilitating multiple antimicrobial mechanisms simultaneously. These include physical disruption of microbial cell membranes through direct contact, generation of reactive oxygen species (ROS) that induce oxidative stress, release of metal ions that interfere with cellular functions, and penetration into cells causing damage to intracellular components such as DNA and proteins.[18] This multifaceted mode of action makes nanomaterials highly effective in killing a broad spectrum of bacteria, including antibiotic-resistant strains, and reduces the likelihood of microbes developing resistance. Furthermore, the shape and size of nanoparticles influence their antimicrobial efficiency by affecting their surface reactivity and ability to interact with microbial membranes. Nanomaterials can also be engineered as carriers for targeted drug delivery, improving efficacy and reducing the side effects of antimicrobial agents. These attributes collectively establish nanomaterials as powerful agents for antimicrobial disinfection beyond their photocatalytic uses.[19,20]

Graphitic carbon nitride (g-$C_3N_4$) has attracted significant interest in recent years as an effective metal free polymeric photocatalyst for environmental remediation and energy conversion owing to its excellent thermal stability, chemical robustness, and favorable band structure.[21] Despite these advantages, g-$C_3N_4$ faces several limitations such as strong particle agglomeration especially in the bulk phase, marginal light absorption and a tendency for rapid recombination of photogenerated charge carriers.[22] Recent efforts to enhance the photocatalytic efficiency of g-$C_3N_4$ has introduced several innovative strategies, among which the direct pyrolysis of 3,5-diamino-1,2,4-triazole represents a novel approach.[23] This method, while effective, involves complex structural properties and chemistry that can limit scalability and reproducibility. In response, nitrogen enriched carbon nitride materials from the same class, specifically g-$C_3N_5$, have gained attention as next-generation photocatalysts. Distinguished by a higher nitrogen content and the integration of triazine rings with electron-rich sites within its structure, g-$C_3N_5$ displays altered physicochemical and electronic properties that enhance its suitability for advanced photocatalytic applications. Notably, its more negative conduction band potential (CB) compared to that of the $O_2/H_2O_2$ redox couple makes it particularly effective for green energy processes such as $H_2O_2$ production.[24,25] Furthermore, g-$C_3N_5$, with its enhanced nitrogen content within the triazine units, exhibits a broader conjugated structure, resulting in a narrower bandgap, improved electrical properties, and superior thermodynamic stability compared to g-$C_3N_5$. However, pure g-$C_3N_5$ has certain limitations, such as sluggish electron–hole pair separation, slow charge transfer dynamics, and a limited oxygen reduction capacity. To overcome these challenges and enable its photocatalytic capability, various strategies, such as morphological control, heterojunction formation, and structural modification, have been explored.[26,27]

Zinc indium sulfide ($ZnIn_2S_4$), a widely recognized p-type ternary chalcogenide, has drawn substantial interest in photocatalysis owing to its notable electrical and optical properties, broad visible-light absorption, environmental compatibility, and remarkable chemical stability. Its potential application is further enhanced by a favourable bandgap structure (2.34–2.48 eV), non-toxicity, and robust photochemical stability.[28] The layered structure of $ZnIn_2S_4$ specifically arranges Zn and In atoms in different surroundings extending its photocatalytic efficiency, which is further enhanced by $In^{3+}$ with $d^{10}$ electrons.[29–31] Nevertheless, the practical photocatalytic application of pure $ZnIn_2S_4$ is hindered by quick $e^-/h^+$ recombination and the susceptibility of $S^{2-}$ to corrosion.[28] Therefore, to facilitate a synergistic interplay of electrons and holes and to improve catalytic performance through surface morphology optimization, photostability enhancement, and bandgap modification, the development of a suitable heterojunction composite with g-$C_3N_5$ is essential. $ZnIn_2S_4$ with g-$C_3N_4$ nanocomposites with improved photocatalytic performance were successfully synthesized in earlier investigations for several crucial applications.[32–34] Recently, Dai *et al.*[35] constructed an S-scheme $ZnIn_2S_4$/g-$C_3N_4$ heterojunction, where efficient charge separation *via* an internal electric field enabled photogenerated electrons from g-$C_3N_4$ to reduce $O_2$ into $^{\bullet}O_2^-$ and $H_2O_2$. These reactive oxygen species facilitated U(VI) removal without sacrificial agents under aerobic conditions, achieving stability and efficiency. Bo *et al.*[36] developed a Z-scheme $ZnIn_2S_4$/g-$C_3N_4$ photoelectrochemical immunosensor, where photogenerated electrons from g-$C_3N_4$ and holes from $ZnIn_2S_4$ were spatially preserved, enabling efficient charge separation and a high initial photocurrent for sensitive CEA detection. The incorporation of $BiVO_4$ as a photoquencher further reduced electron donor accessibility, resulting in a suppressed background signal and achieving a wide detection range (0.0001–100 ng

 © 2025 The Author(s). Published by the Royal Society of Chemistry

Open Access Article. Published on 18 July 2025. Downloaded on 1/16/2026 6:16:01 PM. This article is licensed under a Creative Commons Attribution-NonCommercial 3.0 Unported Licence.

$mL^{-1}$) with a detection limit as low as 0.03 pg $mL^{-1}$. Zheng *et al.*[37] engineered a 2D/1D $ZnIn_2S_4$/g-$C_3N_4$ hollow heterojunction with a 3 : 1 ratio, where type-II band alignment facilitated directional charge transfer and enhanced electron–hole separation. This morphology-tuned system achieved high photocatalytic $CO_2$ reduction yields of 79.96 μmol per g CO and 17.33 $CH_4$ under visible light without sacrificial agents. Wang *et al.*[38] constructed an S-doped g-$C_3N_4$/$ZnIn_2S_4$ heterojunction with a coral-like porous morphology and an enhanced interfacial electric field, enabling efficient charge separation *via* an S-scheme mechanism. The optimized $S_{0.5}$-CN/ZIS achieved a remarkable hydrogen evolution rate of 19.25 mmol $g^{-1}$ $h^{-1}$ and an AQE of 34.43% at 420 nm, outperforming its undoped counterpart by 2.7 times. Liu *et al.*[39] enhanced syngas-selective $CO_2$ reduction by constructing S-scheme $ZnIn_2S_4$/g-$C_3N_4$ heterojunctions with engineered microenvironments, where C–S bonds facilitated charge flow and In vacancies boosted $CO_2$ adsorption. This dual modulation prompted the formation of COOH and CHO* intermediates, enabling efficient charge utilization and controlled syngas generation under visible light. Liu *et al.*[40] developed $ZnIn_2S_4$/g-$C_3N_4$ S-scheme heterojunctions by loading $ZnIn_2S_4$ nanoparticles onto ultrathin g-$C_3N_4$ nanoplates, forming fast interfacial charge transfer pathways and enhancing carrier separation. The optimized GZIS–CN-0.8 showed a hydrogen evolution rate of 7.431 mmol $g^{-1}$ $h^{-1}$ and 90.2% Light Green SF dye degradation within 120 minutes, outperforming individual components by over 5-fold. Liu *et al.*[41] synthesized a 2D/2D S-scheme B-doped, N-deficient g-$C_3N_4$/$ZnIn_2S_4$ heterojunction, where a built-in electric field and engineered defect sites facilitated efficient charge separation and transfer. The optimized catalyst achieved a hydrogen evolution rate of 2378.8 μmol $g^{-1}$ $h^{-1}$ and over 90% tetracycline degradation, driven by the synergistic effects of boron doping, nitrogen vacancies, and interfacial charge dynamics. Li *et al.*[42] fabricated flower-like CoCN/$ZnIn_2S_4$ on defective g-$C_3N_4$ nanosheets, where defect-induced charge separation and strong interfacial coupling significantly boosted photocatalytic activity. The catalyst achieved a high MB degradation rate constant of 0.0061 $min^{-1}$ up to 7.39 times higher than that of pristine components with TOC removal rates of 85.96% for methylene blue and 75.32% for wastewater, driven primarily by $^{\bullet}OH$ radicals. Cao *et al.*[43] developed a Tb-doped $ZnIn_2S_4$/g-$C_3N_4$ photocatalyst that exhibited enhanced electric field modulation and visible-light absorption, enabling efficient antibiotic degradation. The optimized 150ZIS/TCN degraded tetracycline and tylosin 3.2 and 2.1 times faster than g-$C_3N_4$, respectively, under simulated sunlight, demonstrating rare-earth doping as a powerful strategy for photocatalytic wastewater treatment. In recent developments, nitrogen-rich graphitic carbon nitride (g-$C_3N_5$) has emerged as a promising alternative to conventional g-$C_3N_4$ catalysts. This newer variant offers enhanced properties and broader application potential, surpassing its predecessor in several key aspects. Zeng *et al.*[34] synthesized a g-$C_3N_5$@Sv-$ZnIn_2S_4$ heterojunction with a large surface area, achieving rapid mineralization of 2,4-DCP and reduction of Cr(VI) within 60 minutes *via* efficient charge transfer across the S-type interface. The CZSV-200 composite exhibited degradation kinetics up to 4.03 times higher than those in complex water matrices. Wang *et al.*[44] engineered a $ZnIn_2S_2$–$Co_3O_4$–(SiC@g-$C_3N_5$) triple heterojunction integrating P–N, Z-type, and type-II interfaces to enhance photogenerated charge separation and migration synergistically. This hierarchical structure enabled a remarkable hydrogen evolution rate of 13 655 μmol $g^{-1}$ $h^{-1}$, far surpassing that of binary systems by maximizing electron utilization and minimizing recombination losses. Yan *et al.*[32] developed a ternary $Ni_3S_4$@$ZnIn_2S_4$@g-$C_3N_5$ photocatalyst featuring an integrated type-II and Z-scheme heterojunction that was synthesized *via* hydrothermal and electrostatic self-assembly strategies to boost hydrogen evolution. The dual-junction configuration facilitated efficient carrier separation and directional charge transfer, delivering a high hydrogen evolution rate of 9750 mmol $g^{-1}$ $h^{-1}$ – nearly 11-fold higher than that of pure g-$C_3N_5$. Jagan *et al.*[33] demonstrated a double Z-scheme g-$C_3N_5$/$BiFeO_3$/$ZnIn_2S_4$ heterojunction, showing exceptional photo-Fenton degradation of sulfamethoxazole (97% in 60 minutes) under visible light and $H_2O_2$. The enhanced performance stemmed from efficient $Fe^{2+}$/$Fe^{3+}$ cycling and accelerated charge transfer across the Z-scheme interfaces accompanied by generation of reactive oxygen species such as $^{\bullet}OH$, $^{\bullet}O_2^{-}$, and $^1O_2$.

Despite numerous advancements in $ZnIn_2S_4$ and g-$C_3N_5$-based heterojunction photocatalysts, many of these systems involve complex multicomponent architectures or intricate synthetic procedures that limit scalability and reproducibility. However, there remains a lack of focus on simplified yet efficient binary systems, particularly between these two components.[45] A detailed understanding of the photocatalytic process necessitates a comprehensive analysis of the underlying reaction mechanisms, with particular emphasis on the migration behaviour of photogenerated charge carriers. To address this, we have developed a straightforward photocatalyst by anchoring $ZnIn_2S_4$ nanoflowers directly onto g-$C_3N_5$ nanosheets, offering a structurally simple yet functionally robust platform for efficient photocatalytic applications. In this work, a series of $ZnIn_2S_4$/g-$C_3N_5$ nanocomposites were fabricated. The g-$C_3N_5$ nanosheets were synthesized *via* a straightforward thermal polymerization method followed by ultrasonic exfoliation, while $ZnIn_2S_4$ was grown *in situ* on the g-$C_3N_5$ nanosheets using a hydrothermal technique at varying weight percentages. The nanocomposites were evaluated for their multifunctionality in photocatalytic ciprofloxacin degradation and hydrogen peroxide production. The structural and functional integrity of the catalysts was validated through a range of analytical techniques. Furthermore, antibacterial performance was assessed using the zone of inhibition method, demonstrating effective activity against *B. subtilis* and *E. coli*. This study provides a comprehensive evaluation of the nanocomposites' antibacterial and photocatalytic capabilities, with a specific focus on the heterojunction construction and the various parameters influencing photocatalytic efficiency. The electron transfer mechanism of photogenerated carriers in the $ZnIn_2S_4$/g-$C_3N_5$ system was investigated through redox photocatalytic reactions, employing ciprofloxacin as the model contaminant.

Open Access Article. Published on 18 July 2025. Downloaded on 1/16/2026 6:16:01 PM.
This article is licensed under a Creative Commons Attribution-NonCommercial 3.0 Unported Licence.

## 2. Experimental section

### 2.1. Reagents

Zinc nitrate hexahydrate (MERCK), indium(III) chloride (Sigma-Aldrich), thioacetamide (Sigma-Aldrich), ammonium chloride (Sigma-Aldrich), absolute ethanol (SRL), methanol (SRL), acetone (MERCK), 3-amino-1,2,4-triazole (Sigma-Aldrich), ciprofloxacin hydrochloride monohydrate (Sigma-Aldrich), sodium hydroxide pellets (MERCK), hydrochloric acid (MERCK), 2-propanol (MERCK), *p*-benzoquinone (MERCK), citric acid (MERCK), dimethyl sulfoxide (MERCK), Aquivion (Sigma-Aldrich), terephthalic acid (LOBA), nitro blue tetrazolium (Sigma-Aldrich), and hydrogen peroxide (Sigma-Aldrich) were used. All the chemicals are of analytical grade and were used without further purification.

### 2.2. Synthesis of g-$C_3N_5$ bulk/nanosheets

g-$C_3N_5$ (CN) was prepared *via* thermal pyrolysis by heating a 1 : 1 ratio of 3-amino-1,2,4-triazole and ammonium chloride at 500 °C for 3 hours, with a controlled ramp rate of 5 °C $min^{-1}$.[9] The resulting bulk CN, characterized by its ochre colour, was finely ground. To achieve nanosheet morphology, the bulk material underwent ultrasonic exfoliation in methanol for 2 hours. The exfoliated CN nanosheets were then separated by centrifugation at 8000 rpm and subsequently dried at 80 °C overnight to CN nanosheets.[46]

### 2.3. Synthesis of the $ZnIn_2S_4$/g-$C_3N_5$ nanocomposite

To prepare the $ZnIn_2S_4$/g-$C_3N_5$ (ZCN) composite, an appropriate amount of CN powder was first dispersed in 100 mL of distilled water by sonication. An excess amount of thioacetamide (8 mmol) was then added, along with zinc nitrate hexahydrate (1 mmol) and indium chloride (2 mmol), under continuous stirring. The homogenized mixture was then hydrothermally treated under reaction conditions of 180 °C for 12 hours.[28] Upon cooling, a pale yellow ZCN composite was collected *via* centrifugation, followed by water and ethanol cleaning to eliminate sulphur impurities. The final product was then oven-dried at 80 °C overnight. ZCN composites of various $ZnIn_2S_4$ percents (5%, 10%, and 15%) were synthesized and marked as ZCN-5, ZCN-10, and ZCN-15. Pristine $ZnIn_2S_4$ was synthesized by the same method except for the addition of CN and marked as ZIS. All the synthesis methods are well illustrated in Scheme 1.

### 2.4. Photocatalytic ciprofloxacin degradation

Ciprofloxacin (CIP) was chosen as the model pollutant for evaluating the photocatalytic degradation performance. In a typical experiment, 0.04 g of the ZCN-10 catalyst was added to 20 mL of an aqueous CIP solution (20 ppm). Before photocatalytic reactions, an adsorption–desorption equilibrium of CIP was established in the reacting solution by stirring it for 30 minutes in the absence of light. All the photocatalytic experiments were then conducted on the rooftop of our laboratory facility in Bhubaneswar, Odisha, India, during June. The recorded solar intensity was found to be 856 W $m^{-2}$. The overall light illumination time was 90 minutes; at every 15-minute intervals, 3 mL aliquots were withdrawn, and the sample was separated by centrifugation. The residual amount (in ppm) of CIP was determined using a UV 1900i spectrophotometer, and degradation efficiency ($\eta$) was determined using the formula, $\eta = \left[\frac{C_i - C_f}{C_i}\right]$, where $C_i$ is the initial amount of CIP and $C_f$ is the amount at a given time after irradiation. All results presented are the mean from a minimum of three independent results. Cycling stability tests were performed using ZCN-10 following the standard photocatalytic degradation procedure. After each cycle, the material was recovered by centrifugation, followed by thorough washing with water and ethanol to remove residual contaminants, and then dried before being reused in the subsequent cycle.

### 2.5. Photocatalytic hydrogen peroxide production

Photocatalytic hydrogen peroxide ($H_2O_2$) generation was carried out by dispersing 0.02 g of the catalyst in 50 mL of 10%

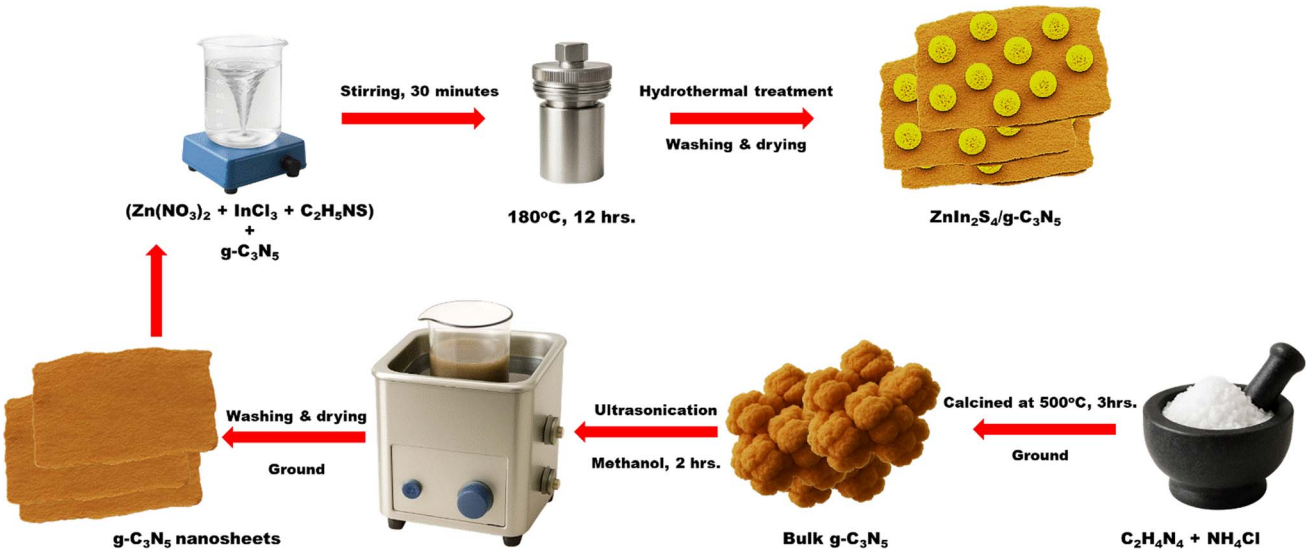


Scheme 1 Schematic illustration for synthesis of $ZnIn_2S_4$, g-$C_3N_5$ and $ZnIn_2S_4$/g-$C_3N_5$ composites.

 © 2025 The Author(s). Published by the Royal Society of Chemistry

Open Access Article. Published on 18 July 2025. Downloaded on 1/16/2026 6:16:01 PM.
This article is licensed under a Creative Commons Attribution-NonCommercial 3.0 Unported Licence.

isopropanol. The suspension was sonicated for 10 minutes to achieve homogeneity. A specifically designed photocatalytic setup, with a water-circulated double-jacketed reactor connected to a 300 W xenon lamp emitting visible light ($\lambda > 420$ nm), was used for the experiments. To provide a continuous oxygen supply for the reduction process, $O_2$ gas was bubbled into the mixture throughout the reaction. During irradiation, 3 mL samples were collected at every 15-minute intervals for 90 minutes. After each sampling, the catalyst was removed *via* centrifugation. The $H_2O_2$ concentration in the collected sample was combined with 1 mL 0.4 M potassium iodide (KI), and 1 mL 0.1 M potassium hydrogen phthalate (KHP). After resting for about 20 minutes, a yellow colouration developed with intensity corresponding to the $H_2O_2$ concentration. The final mixture was diluted, and its absorbance at 350 nm was recorded using a UV-1900i spectrophotometer.

### 2.6. Antibacterial activity

The antibacterial activity of ZIS, CN, ZCN-5, and ZCN-10 composites was evaluated using agar well diffusion, where freshly cultured Gram-positive *B. subtilis* and Gram-negative *E. coli* were employed for the assay. Initially, 20 mL of Mueller Hinton Broth (MHB) solution was taken to which the bacterial strain was sub-cultured overnight. Then sterile Petri dishes were prepared using 20 mL of Mueller Hinton Agar (MHA) which was gelled at room temperature, after which the bacterial strain was uniformly spread on the surface of the plate. Then with the help of a sterile cork borer 6 mm-sized wells were made, and 60 μL of each composite sample, prepared at 10 mg $mL^{-1}$, was introduced into the wells. The plates were then kept undisturbed at 37 °C for incubation overnight, and the inhibition zones were measured in millimeters.

### 2.7. Electrochemical measurements

5 mg of the catalyst sample was homogenized in 100 μL of methanol, followed by the addition of 5 μL of Aquivion as a binder. The sample mixture was further ultrasonicated for 10 minutes to ensure uniform homogeneity of the catalyst. The suspension was then applied onto a 1 × 1 cm fluorine-doped tin oxide (FTO) electrode using a simple drop-casting method. After coating FTO was left undisturbed to dry overnight at 60 °C. The as-prepared FTO-supported uniform catalyst film was taken as a working electrode for all the electrochemical measurements.

Electrochemical measurements were done using a standard three-electrode setup, with a reference electrode (saturated calomel), counter electrode (platinum wire), and FTO film as a working electrode. 0.2 M $Na_2SO_4$ was taken as electrolyte and purged with nitrogen to remove all the dissolved oxygen. Electrochemical impedance spectroscopy (EIS) and Mott–Schottky measurements were conducted at an applied potential of 0.2 V, using a 2 mV AC signal.

### 2.8. Sample characterization

A comprehensive analysis of the composite was conducted using various analytical techniques. The crystallographic studies were done using X-ray diffraction (XRD) on Panalytical X'Pert Pro employing Cu Kα ($\lambda = 1.5406$ Å) with an angle of 5° to 80°. Functional groups were identified by analyzing molecular

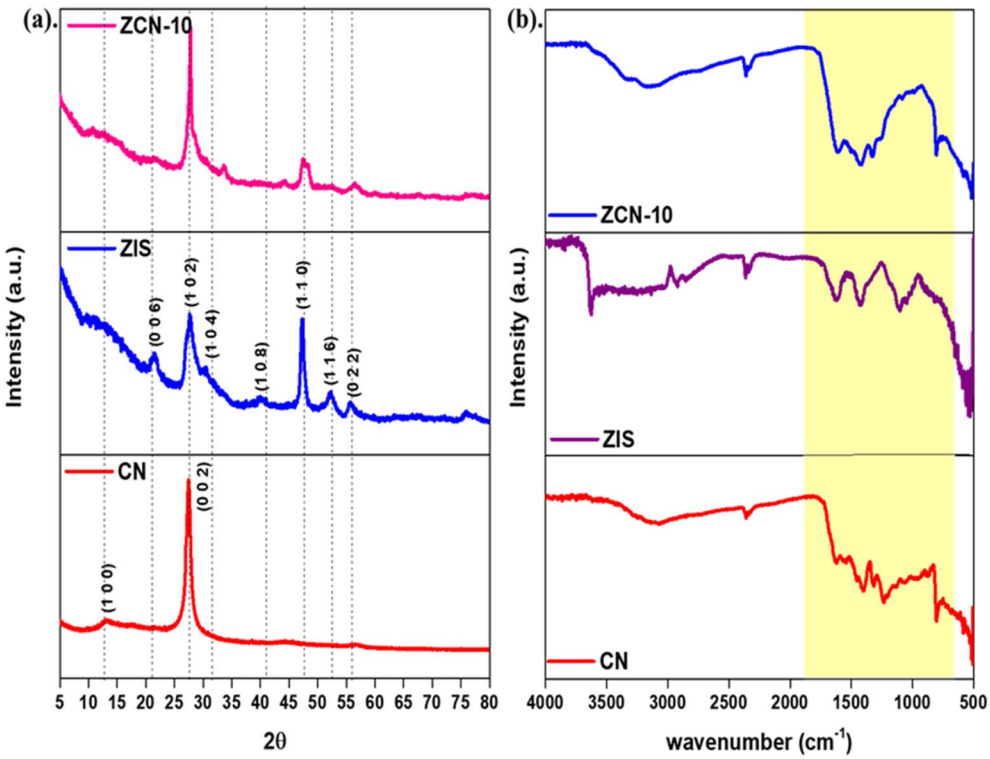


Fig. 1 (a) XRD analysis of ZIS, CN and ZCN-10. (b) FTIR spectra of ZIS, CN and ZCN-10.

Open Access Article. Published on 18 July 2025. Downloaded on 1/16/2026 6:16:01 PM.
This article is licensed under a Creative Commons Attribution-NonCommercial 3.0 Unported Licence.

vibrations through Fourier-transform infrared spectroscopy (FT-IR), carried out on a Spectrum 2 (PerkinElmer) instrument. For this, pellets were prepared by mixing the sample with potassium bromide (KBR), targeting the absorption range of 600–4000 $cm^{-1}$. Surface morphology was examined using a Zeiss Gemini SEM450 Field Emission Microscope (FE-SEM) and a JEOL JEM2100 PLUS Transmission Electron Microscope (TEM). Optical properties were studied using UV-Vis Diffuse Reflectance Spectroscopy (UV-DRS) in the range 200–800 nm, recorded on a LAMBDA 750 UV-Vis-NIR Diffuse Reflectance Spectrophotometer (DRS) (PerkinElmer), with boric acid as a reference. Photoluminescence spectra (PL) were acquired at room temperature using an EDINBURGH FLS 1000 fluorescence spectrophotometer. Electrical measurements were carried out using Ivium electrochemical workstations.

## 3. Results and discussion

### 3.1. Crystallographic and functional group analysis

X-ray diffraction (XRD) analysis of CN, ZIS, and ZCN-10 is depicted in Fig. 1a. In the XRD pattern of CN, two intense peaks at 12.8° and 27.6° indicate (100) and (002) planes, which are attributed to the in-plane conjugated aromatic C–N bonds likely in g-$C_3N_4$ corresponding closely to JCPDS no. 01-087-1526.[47] The characteristic diffraction planes of ZIS with (006) at 21.6°, (102) at 27.7°, (104) at 30.37°, (108) at 39.64°, (110) at 46.9°, (116) at 51.82°, and (022) at 55.86° planes are observed which indicates the successful formation of the hexagonal ZIS structure closely corresponding to JCPDS no. 65-2023.[48] The XRD pattern of ZCN-10 exhibits diffraction planes corresponding to both CN and ZIS. This indicates that the incorporation of components does not significantly alter their respective crystallinities. In addition to crystallographic studies, Fig. 1b illustrates the FTIR spectrum of the modified and unmodified ZIS and CN composites. In addition to the XRD pattern, the FTIR spectrum of the pure and composite forms of CN, ZIS and ZCN-10 are presented. A wide absorbance peak for the N–H stretching vibrations of the triazine rings in graphitic carbon nitride and the O–H stretching of adsorbed water molecules was noted at 3075 $cm^{-1}$. Characteristic peaks corresponding to aromatic C–N stretching vibrations, commonly found in triazine derivatives, appear within the range of 1138 to 1623.77 $cm^{-1}$. Notably, the stretching vibrations of C–N at 1236.44 $cm^{-1}$ and C=N bonds at 1623.77 $cm^{-1}$ were obtained.[49] Moreover, a strong absorption band centered at 806 $cm^{-1}$ is observed, corresponding to the bending mode of the triazine ring, indicative of the in-plane breathing mode of the heptazine units. These spectral features collectively confirm the successful formation of the CN structure, consistent with previous literature.[9,50] The successful synthesis of the ZCN-10 composite is further corroborated by FTIR analysis, which reveals consistent spectral features with the individual components. Notably, the characteristic peak at 806 $cm^{-1}$, corresponding to the triazine ring bending vibration, appears reduced in the composite. This attenuation is likely due to the formation of ZIS nanoflowers on the CN surface, which partially obscures or disrupts the vibrational mode.

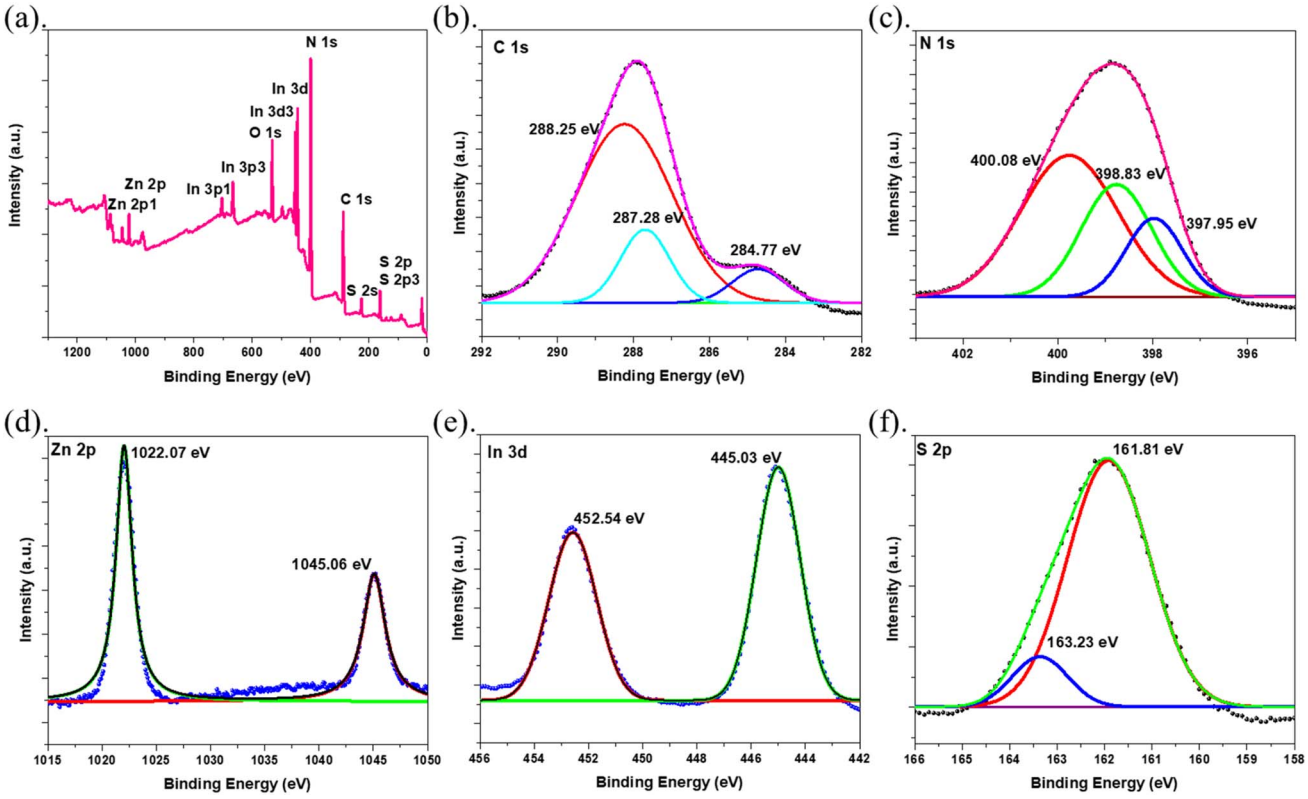


Fig. 2 (a) XPS survey of ZCN-10. (b) C 1s, (c) N 1s, (d) Zn 2p, (e) In 3d, and (f) S 2p XPS spectra.

 © 2025 The Author(s). Published by the Royal Society of Chemistry

Open Access Article. Published on 18 July 2025. Downloaded on 1/16/2026 6:16:01 PM.
This article is licensed under a Creative Commons Attribution-NonCommercial 3.0 Unported Licence.

Additionally, weak absorption peaks obtained at 1396 and 1629 $cm^{-1}$ are attributed to hydroxyl groups and surface adsorbed water molecules associated with the primitive ZIS structure. These observations support the effective integration of ZIS with CN in the composite material.[51]

### 3.2. X-ray chemical state and surface composition analysis

Furthermore, the XPS spectra provide clear evidence for the successful integration of ZIS onto CN nanosheets, as indicated by the survey scan for the ZCN-10 composite in Fig. 2a, which displays distinct signals for C, N, Zn, In, and S, confirming the composite's elemental composition. The high-resolution C 1s spectrum (Fig. 2b) reveals peaks at 284.77, 287.28, and 288.25 eV, corresponding to C–C, C–N, and C=N environments, respectively, characteristic of the graphitic carbon nitride framework.[52] In the N 1s region (Fig. 2c), peaks at 397.95, 398.83, and 400.08 eV are attributed to pyridinic, triazine, and amino nitrogen species, reflecting the diverse nitrogen environments in the carbon nitride matrix.[53] The Zn 2p and In 3d (Fig. 2d and e) spectra show binding energies at 1022.07 and 1045.06 eV and 445.03 and 452.54 eV, respectively, which are slightly shifted compared to their pure phases, indicating strong electronic interactions and possible charge transfer at the ZCN-10 interface. The S 2p spectrum (Fig. 2f) with peaks at 161.81 and 163.23 eV confirms the presence of sulfide species from ZIS.[28] Collectively, these features demonstrate the formation of a well-coupled heterojunction, where the observed shifts

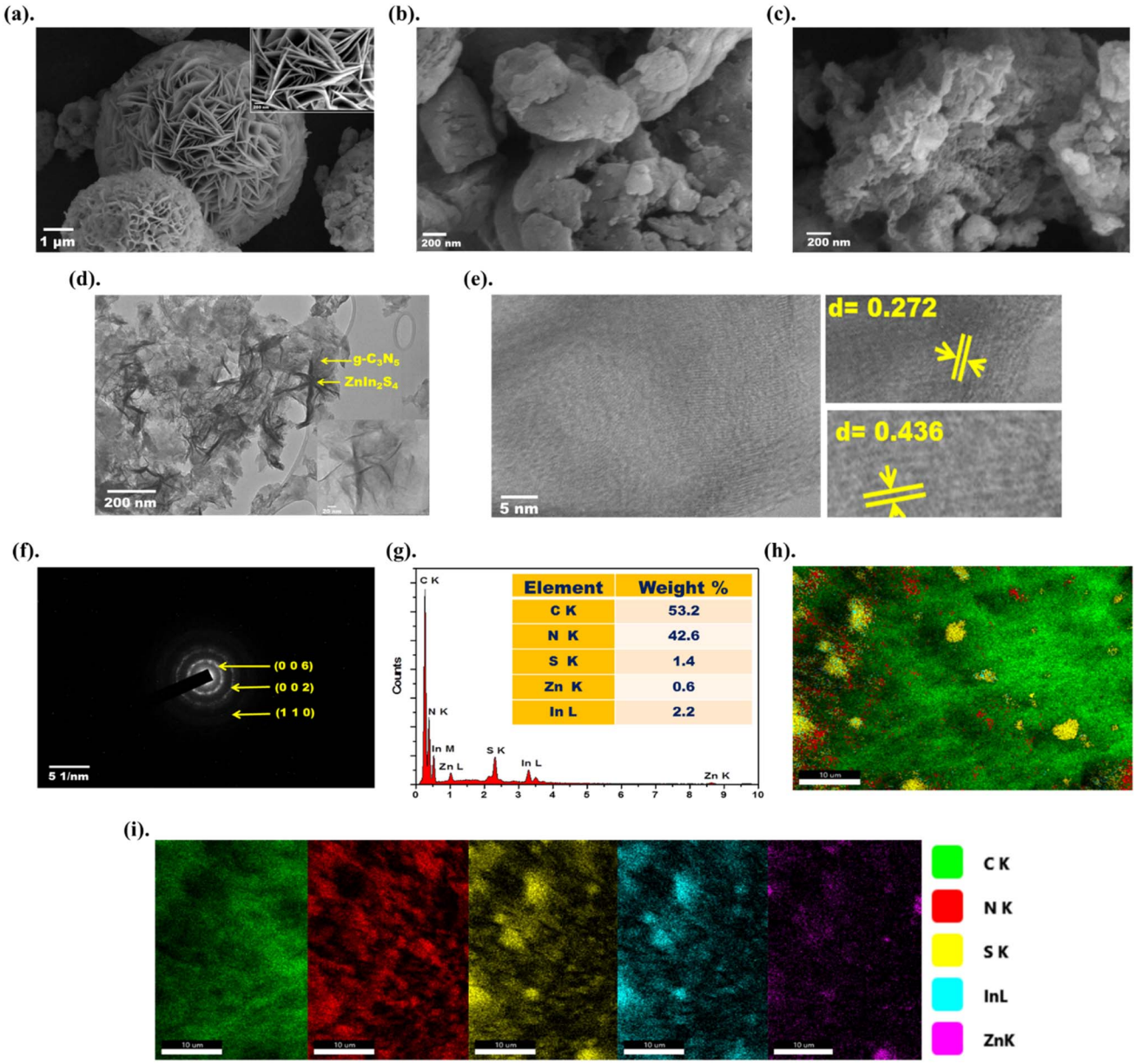


Fig. 3 (a) FE-SEM image of ZIS, (b) FE-SEM image of CN, (c) FE-SEM image of ZCN-10, (d and e) HR-TEM images of ZCN-10, (f) SAED pattern, (g) EDAX spectra, and (h), (i) colour mapping of the ZCN-10 composite.

Open Access Article. Published on 18 July 2025. Downloaded on 1/16/2026 6:16:01 PM.
This article is licensed under a Creative Commons Attribution-NonCommercial 3.0 Unported Licence.

in binding energies suggest enhanced interfacial charge transfer, which is beneficial for improving the composite's photocatalytic properties.

### 3.3. Morphological analysis

To investigate the microstructure and morphology of CN, ZIS, and ZCN-10, analyses such as FE-SEM, TEM, HR-TEM, and EDAX were employed. The ZIS structure, as shown in Fig. 3a, exhibits a three-dimensional nanoflower-like morphology.[54] In contrast, Fig. 3b reveals that the pristine CN features a typical nanosheet-like structure with a smooth surface.[55] Its pliable nature and partially flake-like edges are attributed to the thermal condensation polymerization process at high temperatures followed by ultrasonic exfoliation. With this large surface area of CN nanosheets, a mixed sheet-like morphology emerges, as evidenced in the FE-SEM and TEM images (as shown in Fig. 3c and d). The HR-TEM analysis (Fig. 3e) further highlights lattice fringes corresponding to both ZIS and CN at specific interplanar spacing with mixed phase structures, while the SAED pattern (Fig. 3f) confirms the corresponding indexed planes. Additionally, EDAX data (Fig. 3g) and color mapping (Fig. 3h and i) along with HR-TEM images confirm the uniform distribution of ZIS over CN nanosheets.[56]

### 3.4. Optical and electrochemical analysis

UV DRS was utilized to study the photophysical properties of CN, ZIS, and ZCN-10, as depicted in Fig. 4a. The synthesized materials demonstrated broad optical absorption spanning the UV and visible regions, suggesting their suitability for photocatalytic applications under visible light. The absorption edges for pure CN and ZIS were identified near 438 nm and 750 nm, respectively.[9,51] Incorporating ZIS into CN resulted in a noticeable blue shift in the absorption edge, along with a marked increase in light absorption across a spectrum of 200–800 nm. This enhancement highlights the synergistic interactions between the components and improved light-harvesting efficiency of the composite. The inset of Fig. 4b shows Tauc plots (Kubelka–Munk)[56] to calculate the optical bandgaps of CN, ZIS, and the ZCN-10 composite based on eqn (1),

$$\alpha h\nu^{\gamma} = \beta(h\nu - E_g) \tag{1}$$

where $\alpha$ denotes the absorption coefficient, $h\nu$ denotes photon energy, and $\gamma$ represents the type of electronic transition; $\gamma = 1/2$ corresponds to an allowed indirect transition, while $\gamma = 2$ corresponds to an allowed direct transition. $\beta$ denotes the proportionality constant and $E_g$ denotes the bandgap in eV. As illustrated in Fig. 3b the bandgaps of CN (1.79 eV), ZIS (2.24 eV), and ZCN-10 (1.91 eV) which are consistent with values previously reported in the literature.[9,51,57] The bandgap of the composite is lower than that of pristine ZIS but higher than that of CN, indicating that coupling of ZIS and CN can effectively improve the optical activity, broaden the visible-light response, and enhance the photocatalytic performance.

Photoluminescence (PL) spectral analysis was conducted to gain insights into the charge separation efficiency of carrier species ($e^-/h^+$) in the individual catalysts and their composite

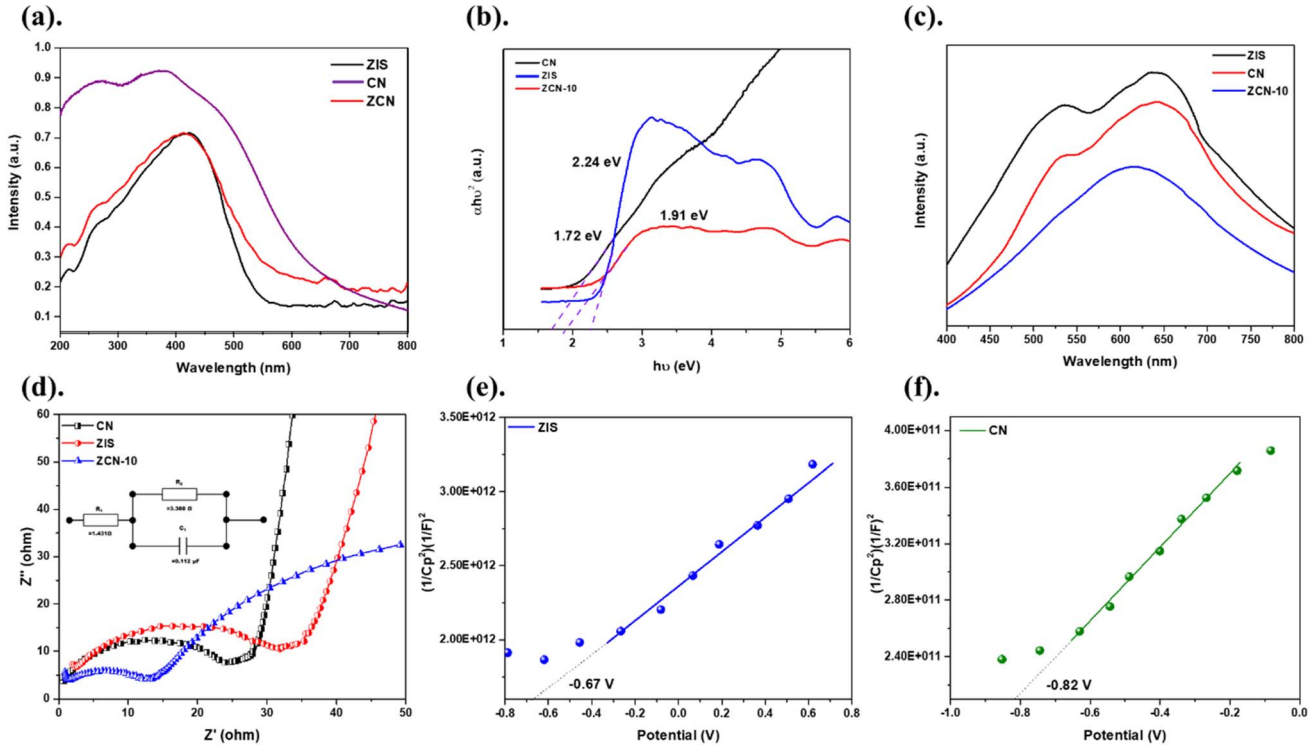


Fig. 4 (a) UV-DRS spectra, (b) Tauc plots for bandgap estimation, (c) PL spectra, (d) EIS Nyquist plots, (e and f) Mott–Schottky plots for the developed catalysts.

 © 2025 The Author(s). Published by the Royal Society of Chemistry

Open Access Article. Published on 18 July 2025. Downloaded on 1/16/2026 6:16:01 PM.
This article is licensed under a Creative Commons Attribution-NonCommercial 3.0 Unported Licence.

form. The intensity of the PL signal is directly related to the rate at which electron–hole pairs recombine; stronger PL signals generally imply a higher recombination rate, which in turn reduces the photocatalytic efficiency. The results obtained from PL analysis (as shown in Fig. 4c) aligned well with the findings from UVDRS, reinforcing the conclusion that lower PL intensities correspond to more effective charge separation.[58] In the study, the fluorescence emission spectra of ZIS, CN, and their composite ZCN-10 were recorded at an excitation wavelength of 320 nm. ZIS exhibited a pronounced emission peak, suggesting a significant rate of electron–hole recombination, which limits its photocatalytic performance. CN, on the other hand, showed a moderately lower emission peak, indicating relatively improved but still limited charge separation ability. Interestingly, when ZIS and CN were integrated to form the ZCN-10 heterojunction, a substantial decrease in PL intensity was observed.[59,60] This notable reduction in fluorescence is attributed to the synergistic interaction between the two semiconductors, which facilitates more efficient spatial separation of carrier species at the heterojunction interface, thereby significantly suppressing recombination and enhancing the overall photocatalytic performance of the composite.[55]

Complementary to the PL study, the electrochemical impedance spectroscopy (EIS) analysis offers additional insight into the charge transfer processes of the CN, ZIS, and ZCN-10 samples. As depicted in Fig. 4d, the Nyquist plot of the ZCN-10 composite displays the smallest semicircle among all samples,[61] which reflects a notably lower charge transfer resistance at the electrode–electrolyte interface compared to CN and ZIS. This reduced resistance indicates that ZCN-10 enables more efficient separation and migration of photogenerated charge carriers, a factor that is closely associated with its enhanced photocatalytic performance.[9,50,51] An equivalent circuit model used to interpret the EIS data, shown in the inset of the plot, consists of a series resistance ($R_1$), in series with a parallel combination of a charge transfer resistance ($R_2$), and a double-layer capacitance ($C_1$). For ZCN-10, the extracted values ($R_1$ = 1.431 Ω, $R_2$ = 3.338 Ω, and $C_1$ = 0.122 μF) confirm a substantial decrease in interfacial resistance relative to the individual CN and ZIS materials. This result underscores the beneficial effect of the composite heterojunction structure, which facilitates rapid interfacial electron transfer and effectively suppresses charge recombination.[58]

In addition to the determination of bandgaps for all the materials, their band edge positions were also estimated with the help of Mott–Schottky plots. This was done by extrapolating to $C^{-2} = 0$ at a frequency of 1000 Hz. As shown in Fig. 4e and f the Mott–Schottky plots exhibit positive slopes, indicating that both CN and ZIS behave as n-type semiconductors. Relative to the normal hydrogen electrode (NHE) at pH 7, the flat band potentials were found to be −0.83 V for CN and −0.67 V for ZIS. Given that the CB of an n-type semiconductor is close to its flat band potential[56,57] the CB positions for CN and ZIS are inferred to be approximately −0.83 V and −0.67 V, respectively which are in good accordance with previous literature.[51,62] Furthermore, the VB band edge positions can be calculated from eqn (2):

$$E_{CB} = E_{VB} - E_g \tag{2}$$

where $E_{CB}$ is conduction band edge potential in V, $E_{VB}$ is valence band edge potential in V, and $E_g$ is the bandgap energy for any semiconducting material. Based on the bandgap values presented in Fig. 4e and f, the VB energies of CN and ZIS are demonstrated to be +0.96 V and +1.57 V, respectively.[63,64] These energy band configurations fulfil the essential criteria required for photocatalytic reactions, indicating the suitability of both CN and ZIS for photocatalytic applications.

### 3.5. Photocatalytic ciprofloxacin (CIP) degradation

The photocatalytic breakdown of CIP using the as-prepared CN, ZIS, ZCN-5, ZCN-10 and ZCN-15 catalysts was done under visible light illumination. To investigate the photocatalytic performance a 30-minute adsorption–desorption equilibrium was established between the catalyst and solution in the dark, followed by solar light for 90 minutes. As depicted in Fig. 5a photocatalytic degradation percent followed the order: ZCN-10 > ZCN-15 > ZCN-5 > ZIS > CN. The degradation rate for the composite structure increased by incorporation of ZIS upon CN up to 10% addition and after that, a slight decline in the catalytic activity was observed which refers to the excess incorporation of ZIS that practically hinders light absorption and surface activity on the surface of CN. Thereafter the ZCN interaction was optimized to 10% due to the well-dispersed ZIS supported on the CN nano-structure, which allows substrate binding on the surface of ZIS nanospheres, followed by breakdown at the surface of CN nanosheets.

To examine the impact of pH on photocatalytic activity, experiments were performed at different pH values of 3, 5, 7 and 9. To determine the optimal pH, the photocatalytic activity was checked under the same reaction conditions except for adjusting the pH values for CIP using diluted HCl and NaOH. As illustrated in Fig. 5b, the results show that the enhanced photodegradation of the catalyst occurred at a pH value of 7. Since three possible chemical routes might contribute to drug degradation, it is challenging to analyze how pH influences the effectiveness of the photodegradation process. The deterioration process includes direct reduction through the conduction band, direct oxidation by positive holes, and attacks by hydroxyl radicals. The contribution of each pathway is affected by the substrate and pH. The breakdown rate is increased and peaks are observed at neutral pH due to the intense interaction between the catalyst surface and the cationic form of CIP, which raises the affinity between the drug molecule and the catalyst. The ZCN-10 nanocomposite achieved a maximum photodegradation efficiency of 85.6%, primarily attributed to its negatively charged surface at pH 7, which facilitates strong electrostatic interactions with the cationic and zwitterionic forms of CIP. By improving the drug's adsorption onto the catalyst surface, this interaction promotes more effective charge transfer and the production of reactive species for efficient photodegradation.

After optimizing the earlier parameters, the study of catalytic doses (0.02, 0.04, 0.06, 0.08, and 0.1 grams) was performed to further improve the overall photocatalytic performance. Fig. 5c

Open Access Article. Published on 18 July 2025. Downloaded on 1/16/2026 6:16:01 PM.
This article is licensed under a Creative Commons Attribution-NonCommercial 3.0 Unported Licence.

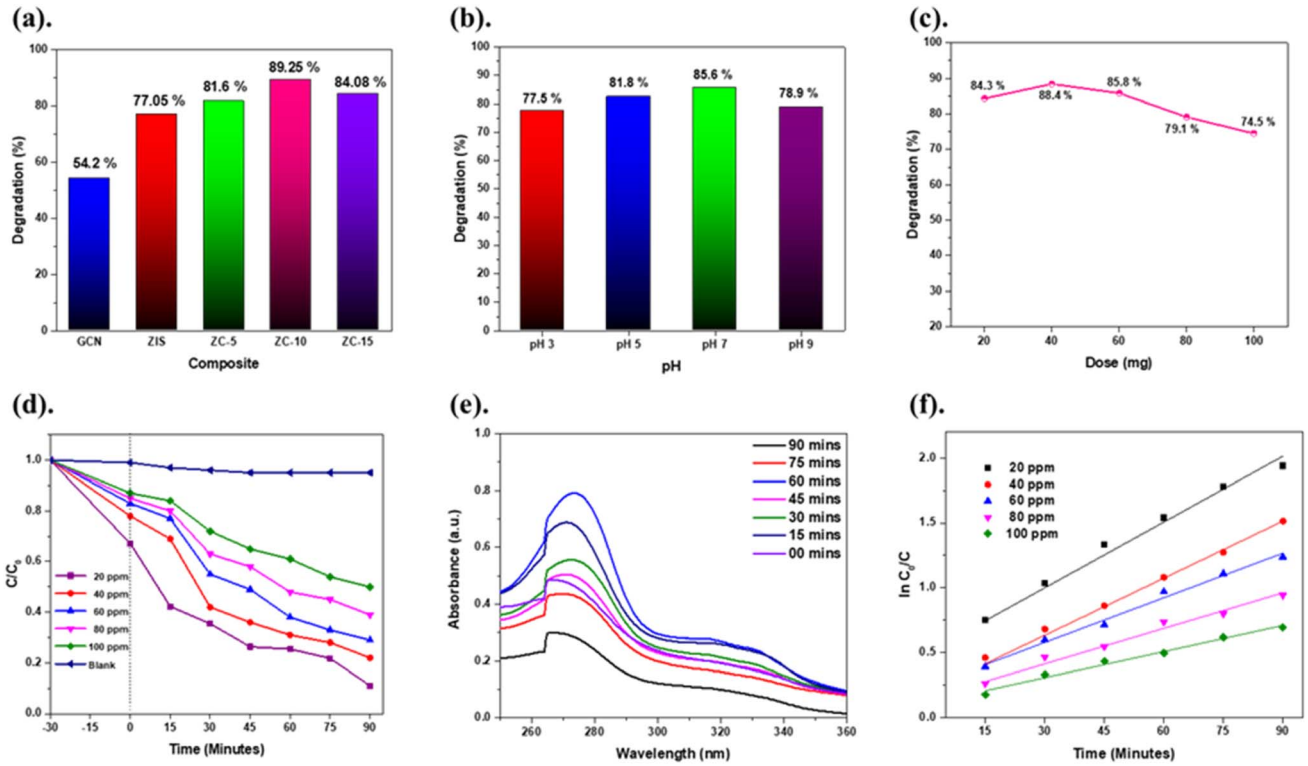


Fig. 5 (a) Effect of various catalysts, (b) effect of solution pH, (c) effect of catalyst dose, (d) effect of solution concentration, (e) absorbance with time, and (f) kinetics with time, for photocatalytic degradation of CIP.

illustrates the interaction between the catalyst doses *vs.* percentage degradation, which demonstrates that the ZCN-10 nanocomposite achieved a maximum degradation of 88.4% at a dosage of 0.04 grams. The graph indicates that as the catalyst dosage increases the graph inclines up to 0.04 grams, and after that point, it marginally lowers. This is because increased charge carrier generation encourages drug breakdown. However, after 0.04 grams of catalyst loading, the efficiency begins to decline. Upon excessive loading of the catalyst, the reacting solution becomes opaque, which slows down the photocatalytic activity and lowers the light harvestation property (the ability of the reactor to absorb photon flux). Furthermore, collisions between surplus catalyst particles lower the degradation percentage when the drug molecules are partially adsorbed onto the catalyst surface.

Fig. 5d illustrates the rate of photocatalytic degradation of CIP over time in a range of concentrations, from 20 to 100 ppm solutions. For 90 minutes, the optimized 20 ppm solution was subjected to an absorption spectral measurement over a wavelength range of 250–450 nm with a 15-minute time interval. As seen in Fig. 5e, the absorption peak intensity, initially observed at 270 nm, progressively decreased over time. For every experiment, the same exposure duration of 90 minutes yielded the highest degradation efficiency. Additionally, pseudo-1st order kinetics were used to explain the rate of CIP degradation over time. The kinetics research illustrates how the CIP concentration affects photodegradation over 15, 30, 45, 60, 75 and 90 minutes, as seen in Fig. 5f. The well-assembled first-order kinetics, eqn (3) and (4), is as follows:

$$K_{\text{app}}t = \ln\frac{C_0}{C_t} \tag{3}$$

$$K_{\text{app}} = \ln\frac{C_0}{C_t} \times \frac{1}{t} \tag{4}$$

The connection between $C_0$ (initial CIP concentration) and $C_t$ (final CIP concentration at time $t$) is depicted, in Fig. 5f, as $C_0/C_t$ as a function of degradation time. The pseudo-1st order kinetics rate constant is represented by the symbol $K_{\text{app}}$. According to the first-order law, the $K_{\text{app}}$ value falls as the concentration solution increases, as seen in Table 1 below.

### 3.6. Antibacterial study

The antibacterial activity of ZIS, CN, ZCN-5, and ZCN-10 was evaluated by measuring the zone of inhibition formed on Mueller–Hinton agar plates. This method allowed for a visual

Table 1 Kinetics study for CIP photodegradation at different concentrations

| Concentration of CIP (ppm) | Time (min) | $K_{\text{app}}$ (min$^{-1}$) | Regression coefficient ($R^2$) |
|---|---|---|---|
| 20 | 90 | 0.024 | 0.99 |
| 40 | 90 | 0.018 | 0.99 |
| 60 | 90 | 0.015 | 0.99 |
| 80 | 90 | 0.014 | 0.97 |
| 100 | 90 | 0.011 | 0.97 |

 © 2025 The Author(s). Published by the Royal Society of Chemistry

Open Access Article. Published on 18 July 2025. Downloaded on 1/16/2026 6:16:01 PM.
This article is licensed under a Creative Commons Attribution-NonCommercial 3.0 Unported Licence.

and quantitative assessment of how effectively each material suppressed the growth of Gram-positive *Bacillus subtilis* (*B. subtilis*) and Gram-negative *Escherichia coli* (*E. coli*) bacteria. As shown in Fig. 6a and b, the ZCN-10 composite exhibited the largest inhibition zone in comparison to ZCN-5 for both the bacteria, indicating superior antibacterial performance against Gram positive and Gram negative bacteria. In contrast, the pristine forms of ZIS and CN showed only slight inhibiting zones for *B. subtilis* whereas for *E. coli* only slight or no inhibition zone was observed, suggesting limited effectiveness when used individually. However, when ZIS was combined with CN to form the ZCN-10 heterostructure, a gradual and significant increase in the inhibition zone was observed. This enhancement, detailed in Fig. 6c, suggests that the formation of a well-structured heterojunction between the two materials played a key role in improving antibacterial efficiency. The improved performance is likely due to enhanced charge carrier separation and increased generation of reactive species, which collectively contribute to more effective bacterial inactivation. Moreover, the composite was found to be more effective against Gram negative *E. coli* compared to Gram positive *B. subtilis* which can be attributed to their differences in cell wall structures.[18] Peptidoglycan layers of Gram-negative bacteria are thinner and their outer membrane is composed of lipopolysaccharides, which are more susceptible to disruption by the ROS generated. In contrast, Gram-positive bacteria have a much thicker peptidoglycan layer that offers greater resistance to oxidative stress. As a result, the ROS species are more effective in penetrating and damaging *E. coli*, leading to a larger inhibition zone compared to *B. subtilis*.[65]

### 3.7. Photocatalytic $H_2O_2$ production

Apart from photocatalytic antibiotic degradation, the adaptability of the catalyst was evaluated using its performance in the oxygen reduction reaction (as shown in Fig. 7a) and followed a trend of ZCN-10 > ZCN-5 > CN > ZIS. An additional external oxygen supply is essential for the oxygen reduction process; it must be adequately supplied to the solution, as the variation in $H_2O_2$ was clearly visible in Fig. 7b making the production more evident. The $H_2O_2$ evolution rate was examined after several sacrificial agents (electron donors) were added to the sample

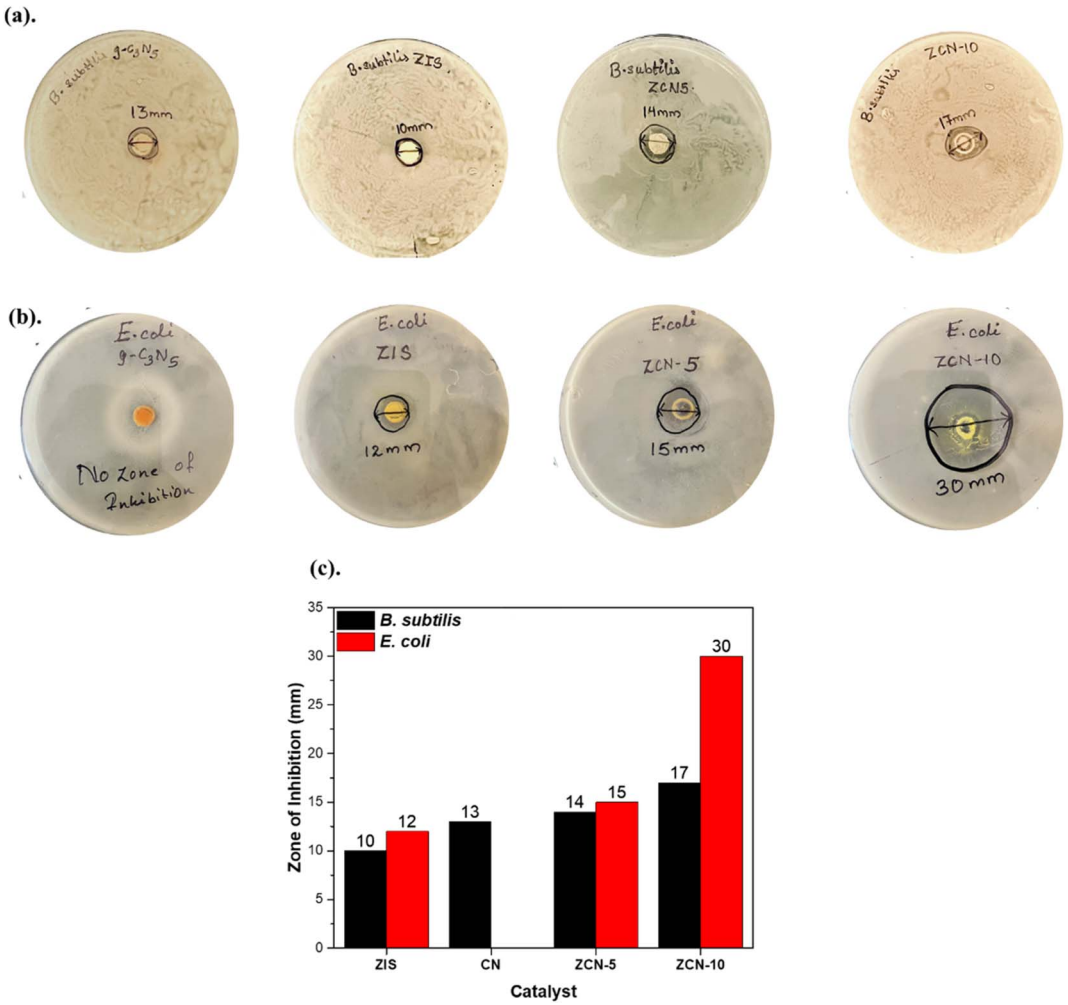


Fig. 6 (a) Inhibition zone for *B. subtilis* with ZIS, CN, ZCN-5, and ZCN-10, (b) inhibition zone for *E. coli* with ZIS, CN, ZCN-5, and ZCN-10, and (c) inhibition zone measurements in mm.

Open Access Article. Published on 18 July 2025. Downloaded on 1/16/2026 6:16:01 PM.
This article is licensed under a Creative Commons Attribution-NonCommercial 3.0 Unported Licence.

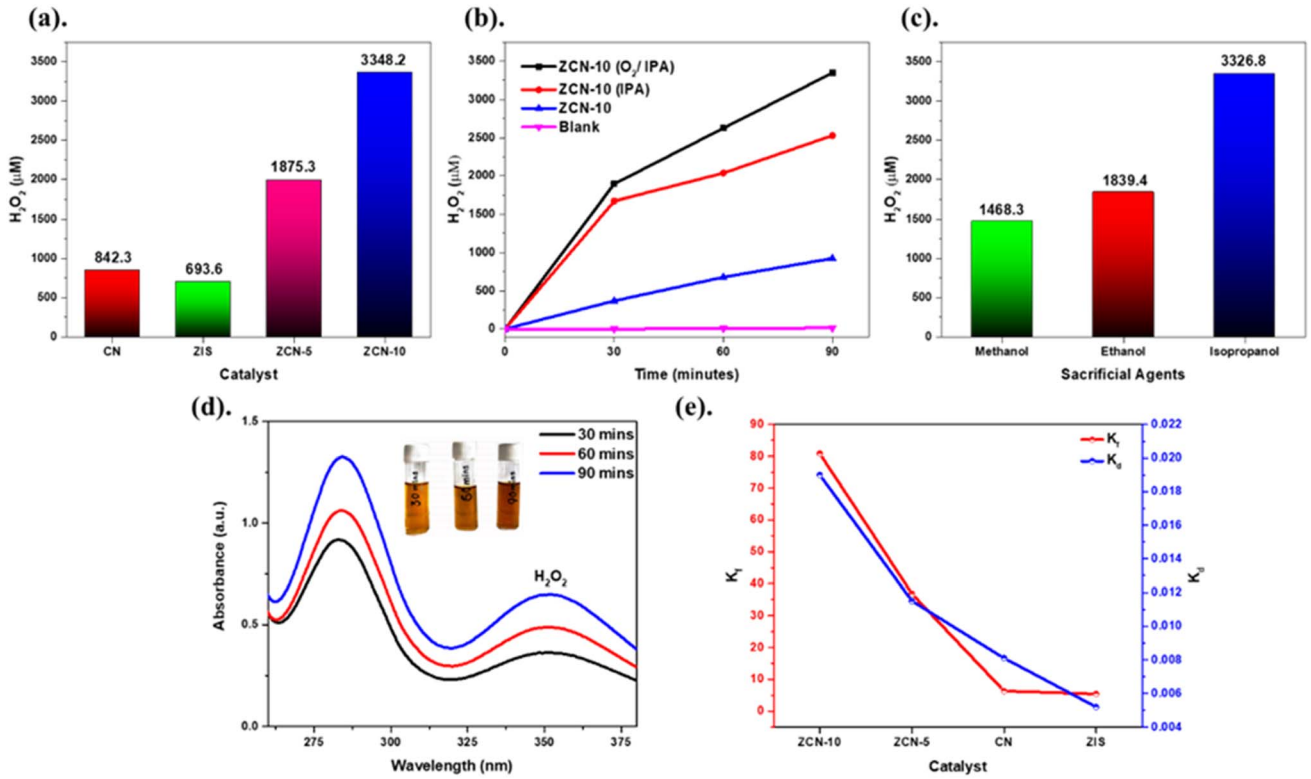


Fig. 7 (a) Effect of various catalysts, (b) effect of $O_2$ purging, (c) effect of sacrificial agents, (d) absorbance peaks for $H_2O_2$ concentration with time, and (e) kinetics study for photocatalytic $H_2O_2$ production.

solution at 10% v/v for further investigations. In comparison to ethanol and methanol, isopropanol was shown to be a superior electron donor,[66] as seen in Fig. 7c. All of the catalysts underwent a similar experiment, and the findings (shown in Fig. 7a) indicated $H_2O_2$ production for ZCN-10 to be 3348.2 μM $L^{-1}$, ZIS to be 693.6 μM $L^{-1}$, and CN to be 842.3 μM $L^{-1}$. On further applying a light intensity of 100 mW $cm^{-2}$ to an irradiated area of 9 $cm^2$, the calculated apparent quantum efficiency (AQE) value was found to be 8.3 for ZCN-10, which is 5.18 times greater than that of ZIS (1.6) and 3.95 times greater than that of CN (2.1). As depicted in Fig. 7d absorbance peaks for $H_2O_2$ at 280 and 350 nm (ref. 12 and 66) indicate the concentration of $H_2O_2$, with the highest $H_2O_2$ generation recorded at 90 minutes for ZC-10. Potential interactions between the generated $H_2O_2$ and other $H_2O_2$ molecules might lead to self-decomposition. Therefore, while investigating photocatalysis, a thorough knowledge of the dynamics involved in $H_2O_2$ production and breakdown is essential.[67–69] To completely understand the dynamic process of photocatalytic $H_2O_2$ formation, it is imperative to investigate these characteristics. Both zeroth-order and first-order kinetics are noted according to eqn (5).[66] According to the data shown in Fig. 7e, ZCN-10 had the highest $K_f$ (rate of formation) values when compared to any catalysts, although the $K_d$ (rate of dissociation) values were noticeably low for all catalysts. These results are consistent with the formation of a heterojunction, which efficiently increases $H_2O_2$ generation.

$$[H_2O_2] = \frac{K_f}{K_d}[1 - \exp(-K_d \times t)] \quad (5)$$

### 3.8. Scavenging test and photocatalytic mechanism

It is often asserted that the photocatalytic reaction requires active species. As shown in Fig. 8a for the ZCN-10 catalyst, a scavenging experiment was conducted using CIP as the model pollutant for photodegradation so as to identify the active reactive oxygen species (ROS) in the photocatalytic mechanism. Optimal photocatalytic conditions were fixed for the experiment. *para*-Benzoquinone (PBQ), dimethyl sulfoxide (DMSO), isopropanol (IPA), and citric acid (CA) were among the scavengers that gathered the superoxide ($^{\bullet}O_2^-$), electrons ($e^-$), the hydroxide ($^{\bullet}OH$), and holes ($h^+$) respectively. Throughout the experiment, the scavenger concentration was kept at 1 mM. The results demonstrate that adding DMSO (34.3%) and PBQ (21.8%) significantly alters the degrading efficiency, but not IPA (48.4%). Nevertheless, the efficiency of ciprofloxacin degradation is also significantly diminished by the addition of CA (46.6%). These results imply that the breakdown of ciprofloxacin is caused by radical species, particularly $e^-$, $h^+$, and $^{\bullet}O_2^-$.

The presence of superoxide radicals ($^{\bullet}O_2^-$) was evaluated using the nitro blue tetrazolium (NBT) assay, which serves as a reliable method for quantifying the species. NBT acts as a probe that undergoes a measurable change in absorbance

 © 2025 The Author(s). Published by the Royal Society of Chemistry

Open Access Article. Published on 18 July 2025. Downloaded on 1/16/2026 6:16:01 PM.
This article is licensed under a Creative Commons Attribution-NonCommercial 3.0 Unported Licence.

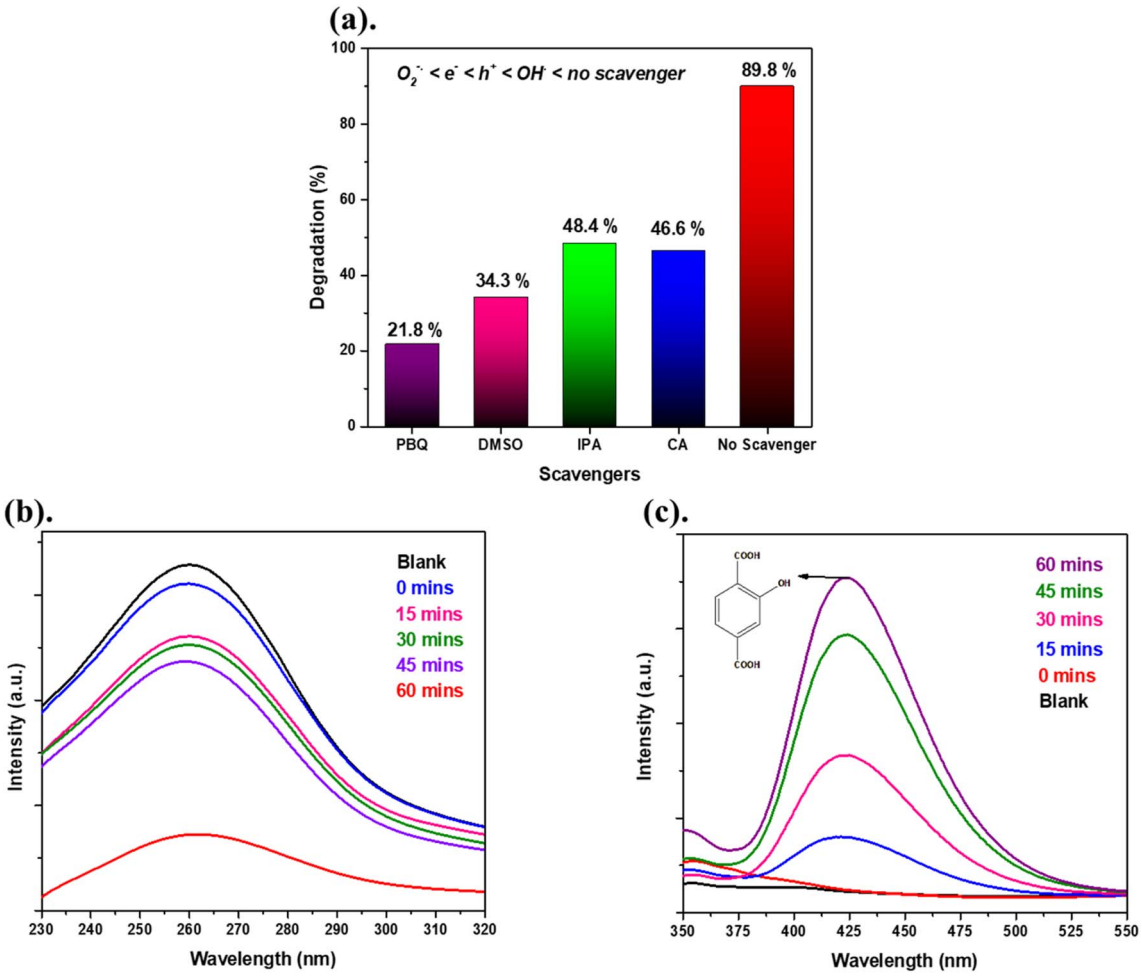


Fig. 8 (a) Effect of scavengers on photocatalytic degradation of CIP, (b) NBT test for superoxide detection, and (c) TA-PL test for hydroxyl radical determination.

when reduced by superoxide radicals, allowing for assessment of photocatalytic activity in different materials.[70] During the experiment, dispersions of the 0.02 g ZCN-10 catalyst at different time intervals were exposed to sunlight in 0.2 mM NBT in 20 mL of 50 mM phosphate buffer solution, and the changes in the NBT concentration were monitored over time using UV-vis spectroscopy. As depicted in Fig. 8b a significant decrease in the maximum absorbance of NBT at 260 nm was observed with increasing time from the blank experiment to 60 minutes, indicating efficient generation of $^{\cdot}O_2^-$ radicals. Similarly, the $^{\cdot}OH$ radical generated during photocatalytic experiments was determined using the terephthalic acid photoluminescence (TA-PL) probe method.[71] In this process, terephthalic acid (TA) reacts specifically with $^{\cdot}OH$ radicals to form a fluorescent compound, 2-hydroxyterephthalic acid (TAOH), which emits characteristic fluorescence at 426 nm when excited at 315 nm. For the experiment, 0.02 g of the catalyst was dispersed in 20 mL 0.4 mM NaOH solution, and the mixture was irradiated with sunlight at different time intervals. The resulting fluorescence intensity of the TAOH solution directly reflected the amount of $^{\cdot}OH$ radicals produced during photocatalysis. As depicted in Fig. 8c with increasing time from blank to 60 minutes the fluorescence peak increased to maximum at 260 nm, indicating its superior ability to generate hydroxyl radicals.

Moreover from the Tauc plots, the bandgaps for ZIS, CN, and ZCN-10 were found to be 2.24 eV, 1.79 eV, and 1.91 eV respectively. The Mott–Schottky plots demonstrate the CB energies of ZIS and CN which were determined to be −0.67 V and −0.83 V, respectively, whereas the VB energies for the individual components were +1.57 V and +0.96 V. CN with a bandgap of 1.79 eV, demonstrating superior visible light harvestation, especially in the red and near-infrared regions extending its optical response up to 670 nm.[72] When combined with ZIS with a bandgap of 2.24 eV and with an absorption edge at around 580 nm (ref. 73) the resulting heterostructures benefit from complementary light absorption properties. This strategic integration broadens the system's overall absorption range, with ZIS capturing higher-energy photons and CN effectively utilizing lower-energy photons. As a result, the composite material achieves enhanced light harvesting and improved charge carrier generation, which contributes to higher photocatalytic performance under solar illumination.[72,73] Integrating

Open Access Article. Published on 18 July 2025. Downloaded on 1/16/2026 6:16:01 PM.
This article is licensed under a Creative Commons Attribution-NonCommercial 3.0 Unported Licence.

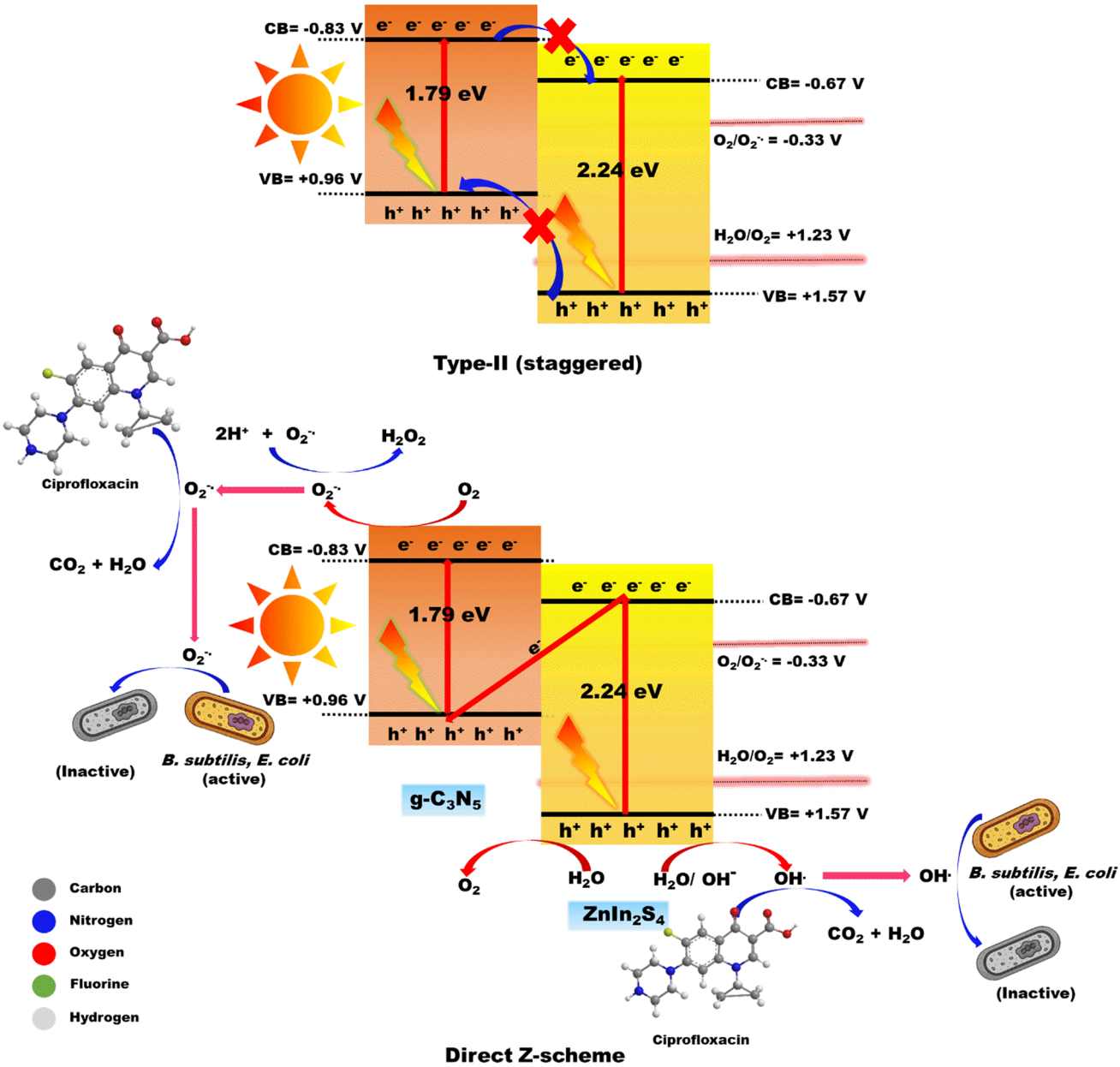


Scheme 2 Plausible mechanism for photocatalytic CIP degradation, $H_2O_2$ production, and antimicrobial activity against *B. subtilis* for the ZCN-10 composite.

ZIS nanoflowers with CN nanosheets significantly boosts photocatalytic efficiency through multiple synergistic effects. The strong interfacial contact between the two components facilitates efficient charge transfer, reminiscent of the hierarchical architectures seen in ZCN-10 systems. These well-defined interfaces are crucial for suppressing electron–hole recombination and enhancing charge carrier mobility.[60] An optimal ZIS loading of around 10% ensures effective heterojunction formation without causing aggregation, thereby preserving accessible active sites and further reducing recombination losses.[74] The distinctive flower-like structure of ZIS contributes to a higher surface area and exposes numerous reactive edge sites, promoting better light harvesting and improved charge separation.[75] Moreover, the alignment of energy bands between the two semiconductors facilitates directional charge flow, favouring a direct Z-scheme heterojunction as shown in Scheme 2, which effectively extends carrier lifetime and enhances photocatalytic performances. Furthermore, a comparative analysis is presented in the accompanying Table 2 to highlight the advantages of the specific heterojunction configuration between g-$C_3N_5$ and $ZnIn_2S_4$, emphasizing the type most favourable for synergistic interaction. The mechanism for a direct Z-scheme can be explained on the basis of charge transfer, which effectively improves charge separation and preserves strong redox potentials. Both semiconductors absorb photons and generate electron–hole pairs in their respective

 © 2025 The Author(s). Published by the Royal Society of Chemistry

Open Access Article. Published on 18 July 2025. Downloaded on 1/16/2026 6:16:01 PM.
This article is licensed under a Creative Commons Attribution-NonCommercial 3.0 Unported Licence.

Table 2 Comparative literature summary of $ZnIn_2S_4$/g-$C_3N_4$-based photocatalysts

| Catalyst | Heterojunction type | Active species | Photocatalytic efficiency | Reference |
|---|---|---|---|---|
| S-doped g-$C_3N_4$/$ZnIn_2S_4$ (S-CN/ZIS) | S-scheme | — | $H_2$ evolution: 19.25 mmol $g^{-1}$ $h^{-1}$ (2.7× CN/ZIS) and AQE = 34.43% @ 420 nm | 38 |
| $ZnIn_2S_4$/g-$C_3N_4$ with tailored microenvironments (ZISCN) | S-scheme | COOH* and CHO* | Syngas generation enhanced by charge modulation & In vacancies | 39 |
| $ZnIn_2S_4$ nanoparticles on g-$C_3N_4$ nanosheets (GZIS–CN-0.8) | S-scheme | — | $H_2$: 7.431 mmol $g^{-1}$ $h^{-1}$ (5.26× ZIS); Light Green SF dye degradation: 90.2% in 120 min | 40 |
| Boron-doped nitrogen-deficient g-$C_3N_4$/$ZnIn_2S_4$ (BDCNN/ZIS) | S-scheme (2D/2D) | — | $H_2$: 2378.8 μmol $g^{-1}$ $h^{-1}$; tetracycline degradation >90%, $k$ = 0.021 $min^{-1}$ | 41 |
| Defective g-$C_3N_4$/$ZnIn_2S_4$ (COCN/ZIS) | Likely type-II | $^{\cdot}OH$, $^{\cdot}O_2^-$, and $h^+$ | MB degradation: $k$ = 0.0661 $min^{-1}$ (6.89× *vs.* g-$C_3N_4$); TOC removal: 85.96% | 42 |
| Tb-doped g-$C_3N_4$/$ZnIn_2S_4$ (ZIS/TCN) | S-scheme | — | TC and TYL degradation 3.2× and 2.1× *vs.* g-$C_3N_4$; enhanced light absorption *via* Tb doping | 43 |
| g-$C_3N_5$@Sv-$ZnIn_2S_4$ (g-$C_3N_5$@Sv-ZIS) | S-type | Photo-generated electrons | 2,4-DCP & Cr(VI) degradation in 60 min; 2.20–4.03× higher kinetics in different waters | 34 |
| $ZnIn_2S_4$–$Co_3O_4$–(SiC@g-$C_3N_5$) | P–N + Z-scheme + type-II (multi-junction) | Photo-generated electrons | $H_2$: 13 655 μmol $g^{-1}$ $h^{-1}$; improved separation *via* synergy of the multijunction | 44 |
| $Ni_3S_4$@$ZnIn_2S_4$@g-$C_3N_5$ | Type-II ($Ni_3S_4$–ZIS) + Z-scheme (ZIS–$C_3N_5$) | Photo-generated electrons | $H_2$: 9750 mmol $g^{-1}$ $h^{-1}$; ∼10.89× *vs.* g-$C_3N_5$ | 32 |
| $C_3N_5$/$BiFeO_3$/$ZnIn_2S_4$ (CBZ-40%) | Double Z-scheme | $^{\cdot}OH$, $^{\cdot}O_2^-$, and $^1O_2$ | SMX degradation: 97% in 60 min using a Vis/$H_2O_2$ system; excellent reusability | 33 |
| $ZnIn_2S_4$/g-$C_3N_5$ ZCN-10 | Z-scheme | $^{\cdot}OH$ and $^{\cdot}O_2^-$ | 88.4% degradation of CIP within 90 min, 3368 μM $L^{-1}$ of $H_2O_2$ under visible light with an AQE = 8.3, and 17 and 30 mm inhibition zones against *B. subtilis* and *E. coli*, respectively | *This work* |

© 2025 The Author(s). Published by the Royal Society of Chemistry

Open Access Article. Published on 18 July 2025. Downloaded on 1/16/2026 6:16:01 PM.
This article is licensed under a Creative Commons Attribution-NonCommercial 3.0 Unported Licence.

bands. The photogenerated electrons from the CB of ZIS migrate and recombine with the holes in the VB band of CN. This selective recombination pathway ensures that the electrons with strong reducing power are retained in the CB of CN, while the oxidizing $h^+$ remains in the VB position of ZIS. These active charge carriers then engage in surface redox reactions where $e^-$ reduce adsorbed $O_2$ to form $^{\bullet}O_2^-$ and $h^+$ oxidize $H_2O$ or $OH^-$ ions to generate $^{\bullet}OH$ radicals. The synergistic action of these reactive species leads to efficient degradation of pollutants, as well as $H_2O_2$ production.[76]

Along with photocatalytic applications, nanocomposites can also be employed for antibacterial disinfection purposes due to their unique physicochemical properties. ZCN-10 like bioactive materials can act as antimicrobial agents to combat bacterial infections. The antibacterial properties of the synthesized composites were assessed using the agar well diffusion method against Gram-positive *B. subtilis* and Gram-negative *E. coli*. The ZCN-10 composite demonstrated superior antibacterial activity compared to pristine ZIS and CN, as evidenced by a larger inhibition zone, indicating enhanced effectiveness against the bacteria. This enhancement is primarily due to the improved generation of reactive oxygen species (ROS) facilitated by the Z-scheme heterojunction formed between ZIS and CN. While ZIS alone has limited antibacterial activity because of its quicker carrier recombination, coupling it with CN promotes efficient separation of photoinduced charge carriers. In the Z-scheme mechanism, the electrons from CN and the holes from ZIS remain active, both of which have strong redox abilities that contribute to higher ROS production. When these ROS, including superoxide and hydroxyl radicals, come in contact with cellular bodies, can disturb the integrity of the bacterial membranes and intercellular components, leading to effective bacterial inhibition. As the ZIS percentage increases, light harvesting and charge carrier dynamics are further optimized, resulting in stronger antibacterial action, with ZCN-10 showing

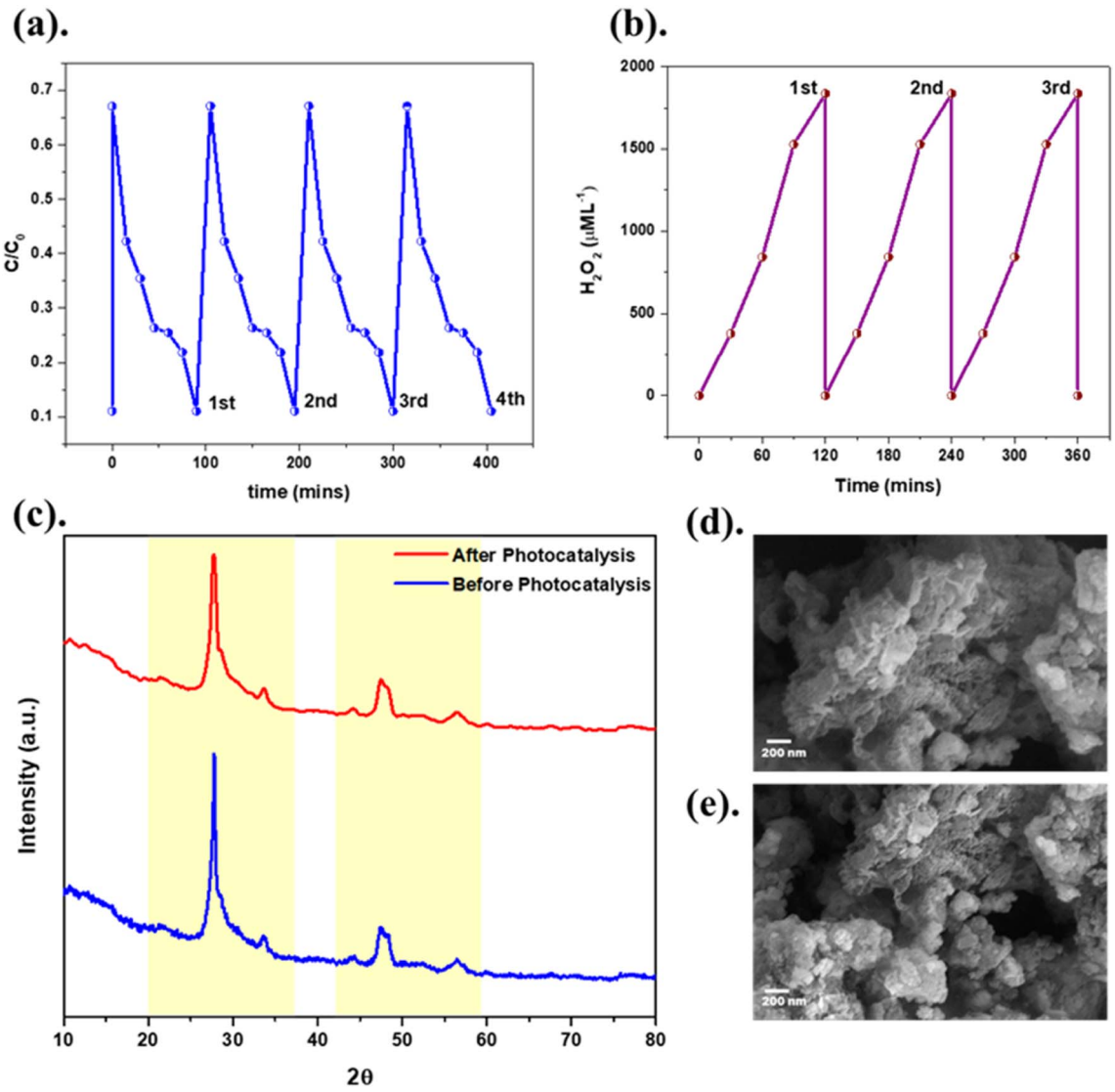


Fig. 9 (a) Reusability test for CIP, (b) reusability test for $H_2O_2$ production, (c) XRD analysis, and (d), (e) FE-SEM images before and after photocatalysis.

 © 2025 The Author(s). Published by the Royal Society of Chemistry

Open Access Article. Published on 18 July 2025. Downloaded on 1/16/2026 6:16:01 PM.
This article is licensed under a Creative Commons Attribution-NonCommercial 3.0 Unported Licence.

the most pronounced effect. The detailed formation of reactive species by photolysis can be explained using eqn (6)–(13):

$$\text{ZCN-10} + h\nu \rightarrow e^- + h^+ \quad (6)$$

$$e^- + O_2 \rightarrow {}^{\bullet}O_2^- \quad (7)$$

$$h^+ + H_2O/OH^- \rightarrow {}^{\bullet}OH \quad (8)$$

$${}^{\bullet}O_2^- + \text{CIP} \rightarrow CO_2 + H_2O \quad (9)$$

$${}^{\bullet}OH + \text{CIP} \rightarrow CO_2 + H_2O \quad (10)$$

$${}^{\bullet}O_2^- + e^- + 2H^+ \rightarrow H_2O_2 \quad (11)$$

$${}^{\bullet}O_2^- + \textit{B. subtilis}, \textit{E. coli}\ (\text{active}) \rightarrow \textit{B. subtilis}, \textit{E. coli}\ (\text{inactive}) \quad (12)$$

$${}^{\bullet}OH + \textit{B. subtilis}, \textit{E. coli}\ (\text{active}) \rightarrow \textit{B. subtilis}, \textit{E. coli}\ (\text{inactive}) \quad (13)$$

### 3.9. Reusability test

Reusability is a key factor in determining the long-term viability and cost-effectiveness of photocatalysts for environmental and industrial applications.[77] In this context, the ZCN-10 catalyst was systematically investigated for its performance across multiple cycles of photocatalytic degradation and hydrogen peroxide production. During degradation experiments, ZCN-10 consistently maintained high efficiency over four consecutive cycles (as shown in Fig. 9a), indicating strong catalytic stability. For $H_2O_2$ production, the catalyst demonstrated steady activity over three cycles (as shown in Fig. 9b), followed by a slight decline in performance. Structural analysis after repeated use confirmed the catalyst's durability. XRD patterns as depicted in Fig. 9c showed only a minimal decrease in peak intensity, reflecting minor changes in crystallinity without any major phase transitions. Moreover, the FE-SEM image from Fig. 9d and e indicated negligible changes in morphology, supporting the structural integrity of the catalyst. These results collectively highlight ZCN-10 as a reliable and recyclable photocatalyst, making it a promising candidate for real-world applications in pollutant degradation and $H_2O_2$ generation.

## 4. Conclusion

In summary, the hydrothermal *in situ* growth of $ZnIn_2S_4$ nanoflowers supported on g-$C_3N_5$ nanosheets successfully produced a Z-scheme heterojunction photocatalyst with enhanced functional properties. The sample with the composition of 10% $ZnIn_2S_4$ with g-$C_3N_5$ (ZCN-10) exhibited efficient charge separation and suppressed electron–hole recombination, attributed to strong interfacial contact within the well-organized hierarchical structure. This photocatalyst demonstrated remarkable activity, achieving 88.4% degradation of ciprofloxacin within 90 minutes at neutral pH, following pseudo-first-order kinetics. This performance highlights its effectiveness in eliminating antibiotic contaminants from water. Additionally, ZCN-10 showed excellent hydrogen peroxide generation, producing 3348.2 μM $L^{-1}$ in 90 minutes using isopropanol as a sacrificial agent, and the reaction mechanism followed a combination of zeroth-order and first-order kinetics indicating potential in green chemical synthesis and oxidative pollutant removal. The catalyst also showed a strong antibacterial effect against *B. subtilis* and *E. coli* evidenced by 17 and 30 mm inhibition zones, respectively surpassing the activity of the individual components, making it suitable for antibacterial disinfection strategies. Mechanistic studies identified superoxide and hydroxyl radicals as the main reactive species in both photocatalytic and disinfection applications. Furthermore, reusability experiments were conducted to check its catalytic lifetime and practical applications, which confirmed that the catalyst was stable across multiple cycles, with minimal structural and morphological changes as observed through XRD and FE-SEM analyses. Overall, the integration of $ZnIn_2S_4$ onto g-$C_3N_5$ offers an excellent approach to tuning their structural, optical, and electrical properties. This modification fosters a synergistic interaction within the Z-scheme heterojunction, significantly enhancing photocatalytic efficiency and establishing ZCN-10 as a highly promising candidate for a wide range of environmental and energy applications.

## Data availability

All data and materials are included in the manuscript.

## Author contributions

Pratyush Kumar Sahu: conceptualization, visualization, writing – original draft, investigation, resources, formal analysis. Aslisha Champati: investigation, formal analysis. Alaka Rath: investigation, formal analysis. Sovanika Pradhan: resources, formal analysis. Abanti Pradhan: visualization, formal analysis. Brundabana Naik: conceptualization, visualization, supervision, writing – review & editing.

## Conflicts of interest

There are no conflicts of interest to declare.

## Acknowledgements

All the authors are thankful to the authority of Siksha 'O' Anusandhan, deemed to be University, and CSIR-Institute of Materials and Minerals Technology, Bhubaneswar, Odisha, India, for providing research facilities to carry out this work.

## References

1 P. K. Sahu, A. Champati, A. Pradhan and B. Naik, *Sustainable Energy Fuels*, 2024, **8**, 1872–1917.
2 Y. Picó, R. Alvarez-Ruiz, A. H. Alfarhan, M. A. El-Sheikh, H. O. Alshahrani and D. Barceló, *Sci. Total Environ.*, 2020, **701**, 135021.

Open Access Article. Published on 18 July 2025. Downloaded on 1/16/2026 6:16:01 PM.
This article is licensed under a Creative Commons Attribution-NonCommercial 3.0 Unported Licence.

3 A. Balakrishnan, M. Sillanpää, M. M. Jacob and D.-V. N. Vo, *Environ. Res.*, 2022, **213**, 113613.
4 C. Trautwein, J.-D. Berset, H. Wolschke and K. Kümmerer, *Environ. Int.*, 2014, **70**, 203–212.
5 C. M. Manaia, *Trends Microbiol.*, 2017, **25**, 173–181.
6 X. Li, J. Xiong, X. Gao, J. Ma, Z. Chen, B. Kang, J. Liu, H. Li, Z. Feng and J. Huang, *J. Hazard. Mater.*, 2020, **387**, 121690.
7 X. Hu, X. Hu, Q. Peng, L. Zhou, X. Tan, L. Jiang, C. Tang, H. Wang, S. Liu, Y. Wang and others, *Chem. Eng. J.*, 2020, **380**, 122366.
8 S. Shen, X. Li, Y. Zhou, L. Han, Y. Xie, F. Deng, J. Huang, Z. Chen, Z. Feng, J. Xu and others, *J. Mater. Sci. Technol.*, 2023, **155**, 148–159.
9 P. K. Sahu, A. Champati, A. Pradhan, N. K. Sahoo and B. Naik, *J. Nanopart. Res.*, 2024, **26**, 261.
10 S. Zhao, S.-S. Shen, L. Han, B.-C. Tian, N. Li, W. Chen and X.-B. Li, *Rare Met.*, 2024, **43**, 4038–4055.
11 X. Li, Q. Liu, F. Deng, J. Huang, L. Han, C. He, Z. Chen, Y. Luo and Y. Zhu, *Appl. Catal., B*, 2022, **314**, 121502.
12 S. Jing, J. Zhao, A. Wang, Q. Ji, R. Cheng, H. Liang, F. Chen, P. Kannan, A. Brouzgou and P. Tsiakaras, *Chem. Eng. J.*, 2024, **479**, 147150.
13 J. Wang, Q. Zhang, F. Deng, X. Luo and D. D. Dionysiou, *Chem. Eng. J.*, 2020, **379**, 122264.
14 J. Song, J. M. Yu, J. H. Ahn, H. Cho, J. Oh, Y. S. Kim, J. Kim, M. Ko, S. Lee, T. J. Shin and others, *Adv. Funct. Mater.*, 2022, **32**, 2110412.
15 A. Wang, H. Liang, F. Chen, X. Tian, S. Yin, S. Jing and P. Tsiakaras, *Appl. Catal., B*, 2022, **310**, 121336.
16 J. Zhao, P. Yan, A. Qureshi and Y. W. Chiang, *Blue-Green Systems*, 2023, **5**, 75–101.
17 L. Wang, C. Hu and L. Shao, *Int. J. Nanomed.*, 2017, 1227–1249.
18 A. Champati, P. K. Sahu, B. Naik and A. Pradhan, *Bionanoscience*, 2025, **15**, 1–34.
19 D. B. Olawade, O. Z. Wada, O. Fapohunda, B. I. Egbewole, O. Ajisafe and A. O. Ige, *Frontiers in Nanotechnology*, 2024, **6**, 1427843.
20 P. Garg, P. Attri, R. Sharma, M. Chauhan and G. R. Chaudhary, *Frontiers in Nanotechnology*, 2022, **4**, 898411.
21 D. Cruz, S. Żółtowska, O. Savateev, M. Antonietti and P. Giusto, *Nat. Commun.*, 2025, **16**, 374.
22 Y. Tong, J. Xia, Y. Hu, Y. He, G. He and H. Chen, *Chem. Commun.*, 2025, **61**, 1509–1532.
23 P. Babu, H. Park and J. Y. Park, *J. Phys. Chem. C*, 2025, **129**, 6129–6137.
24 S. Li, G. Dong, R. Hailili, L. Yang, Y. Li, F. Wang, Y. Zeng and C. Wang, *Appl. Catal., B*, 2016, **190**, 26–35.
25 J. Xiong, X. Li, J. Huang, X. Gao, Z. Chen, J. Liu, H. Li, B. Kang, W. Yao and Y. Zhu, *Appl. Catal., B*, 2020, **266**, 118602.
26 Y. Shen, R. Xu, P. Shan, S. Zhang, L. Sun, H. Xie, F. Guo, C. Li and W. Shi, *Small*, 2024, **20**, 2401566.
27 H. Che, P. Wang, J. Chen, X. Gao, B. Liu and Y. Ao, *Appl. Catal., B*, 2022, **316**, 121611.
28 L. Yang, J. Zhao, Z. Wang, L. Wang, Z. Zhao, S. Li, G. Li and Z. Cai, *Spectrochim. Acta, Part A*, 2022, **276**, 121184.
29 X. Tu, J. Lu, M. Li, Y. Su, G. Yin and D. He, *Nanoscale*, 2018, **10**, 4735–4744.
30 Y. Yan, Z. Chen, X. Cheng and W. Shi, *Catalysts*, 2023, **13**, 967.
31 G. Zhang, H. Wu, D. Chen, N. Li, Q. Xu, H. Li, J. He and J. Lu, *Green Energy Environ.*, 2022, **7**, 176–204.
32 H. Yan, W. Li, H. Yang, Y. Yu, C. Lv, L. Hou, W. Zhang, D. Lin and S. Jiao, *Environ. Res.*, 2024, **248**, 118302.
33 G. Jagan, K. Saravanakumar, J. Li, Y. Yoon and C. M. Park, *Chem. Eng. J.*, 2023, **471**, 144707.
34 Y. Zeng, S. Liu, G. Zhu, Q. Wang, X. Yang and H. Yu, *J. Alloys Compd.*, 2024, **1008**, 176652.
35 Z. Dai, B. Liang, L. Chen, W. Zhang, Y. Gao and L. Li, *Sep. Purif. Technol.*, 2025, **354**, 129241.
36 Y. Bo, L. Li, P. Miao, C. Li, J. Chang, Y. Zhang, Y. Lv, X. Yang, J. Zhang and M. Yan, *Biosens. Bioelectron.*, 2024, **247**, 115926.
37 Z. Zheng, T. Du, P. Chen, Q. Yue, H. Wang, L. Zhou and Y. Wang, *J. Environ. Chem. Eng.*, 2024, **12**, 112971.
38 T. Wang, X. Pan, M. He, L. Kang and W. Ma, *Adv. Sci.*, 2024, **11**, 2403771.
39 Y. Liu, A. Deng, Y. Yin, J. Lin, Q. Li, Y. Sun, J. Zhang, S. Li, S. Yang, Y. Xu and others, *Appl. Catal. B Environ. Energy*, 2025, **362**, 124724.
40 X. Liu, S. Kang, G. Yang, Z. Wang, G. Gao, M. Dou, H. Yang, R. Li, D. Li and J. Dou, *Int. J. Hydrogen Energy*, 2024, **51**, 410–424.
41 J. Liu, Y. Fu, G. Chu, K. Wen, L. Qiu, P. Li, L. Cheng, B. Cao, Y. Tang, X. Chen and others, *Process Saf. Environ. Prot.*, 2024, **191**, 883–896.
42 Y. Li, Y. Chen, H. Lyu and Z. Xie, *J. Photochem. Photobiol., A*, 2024, **457**, 115933.
43 Q. Cao, B. Wang, G. Li, X. Wang, J. Zhang and H. Lv, *J. Environ. Chem. Eng.*, 2024, **12**, 114175.
44 B. Wang, W. Zhang, W. Li, H. Xu, Y. Li, S. Li, X. Huang, S. Jiao, D. Lin and H. Yan, *Surf. Interfaces*, 2025, 106950.
45 Y.-C. Chang, Y.-C. Chiao and C.-J. Chang, *Catalysts*, 2023, **13**, 1187.
46 Z. Ma, W. Guo, K. Zhang, N. Wang, Z. Li and J. Li, *Environ. Sci. Pollut. Res.*, 2023, **30**, 69486–69498.
47 I. Fareed, M. D. Khan, M. Tahir, F. K. Butt and others, *Ceram. Int.*, 2024, **50**, 36004–36017.
48 I. Tateishi, M. Furukawa, H. Katsumata and S. Kaneco, *Catalysts*, 2019, **9**, 681.
49 H. Ghafuri, Z. Tajik, N. Ghanbari and P. Hanifehnejad, *Sci. Rep.*, 2021, **11**, 19792.
50 S. Liu, Y. Bu, S. Cheng, Y. Tao and W. Hong, *J. Water Process Eng.*, 2023, **54**, 104019.
51 Y. Qin, H. Li, J. Lu, Y. Feng, F. Meng, C. Ma, Y. Yan and M. Meng, *Appl. Catal., B*, 2020, **277**, 119254.
52 S. Liu, Y. Bu, S. Cheng and R. Tao, *Diam. Relat. Mater.*, 2023, **136**, 110062.
53 Y. Zhang, T. Cui, J. Zhao, Y. Yan and J. Jiang, *Inorg. Chem. Commun.*, 2022, **143**, 109815.
54 Q. Li, Q. Lu, E. Guo, M. Wei and Y. Pang, *Energy Fuels*, 2022, **36**, 4541–4548.

 © 2025 The Author(s). Published by the Royal Society of Chemistry

Open Access Article. Published on 18 July 2025. Downloaded on 1/16/2026 6:16:01 PM.
This article is licensed under a Creative Commons Attribution-NonCommercial 3.0 Unported Licence.

55 A. Uddin, T. Muhmood, Z. Guo, J. Gu, H. Chen and F. Jiang, *J. Alloys Compd.*, 2020, **845**, 156206.
56 S. Vadivel, S. Hariganesh, B. Paul, G. Mamba and P. Puviarasu, *Colloids Surf., A*, 2020, **592**, 124583.
57 F. Wang, S. Chen, J. Wu, W. Xiang and L. Duan, *Ind. Eng. Chem. Res.*, 2023, **62**, 15907–15918.
58 L. Hou, Z. Wu, C. Jin, W. Li, Q. Wei, Y. Chen and T. Wang, *Nanomaterials*, 2021, **11**, 2483.
59 X. Dang, M. Xie, F. Dai, J. Guo, J. Liu and X. Lu, *Adv. Mater. Interfaces*, 2021, **8**, 2100151.
60 Z. Zhang, K. Liu, Z. Feng, Y. Bao and B. Dong, *Sci. Rep.*, 2016, **6**, 19221.
61 B. Debnath, S. M. Hossain, A. Sadhu, S. Singh, V. Polshettiwar and S. Ogale, *ACS Appl. Mater. Interfaces*, 2022, **14**, 37076–37087.
62 H. Liu, F. Sun, X. Li, Q. Ma, G. Liu, H. Yu, W. Yu, X. Dong and Z. Su, *Composites, Part B*, 2023, **259**, 110746.
63 L. Wang, T. Yang, L. Peng, Q. Zhang, X. She, H. Tang and Q. Liu, *Chin. J. Catal.*, 2022, **43**, 2720–2731.
64 F. Yi, J. Liu, G. Liang, X. Xiao and H. Wang, *J. Alloys Compd.*, 2022, **905**, 164064.
65 S. Ghodsi, A. Esrafili, H. R. Sobhi, R. Rezaei Kalantary, M. Gholami and R. Maleki, *AMB Express*, 2021, **11**, 1–12.
66 A. Balakrishnan, E. S. Kunnel, S. Trivedi, R. Sasidharan, A. Kumar and M. Chinthala, *Ind. Eng. Chem. Res.*, 2024, **63**, 18975–18988.
67 H. Che, J. Wang, X. Gao, J. Chen, P. Wang, B. Liu and Y. Ao, *J. Colloid Interface Sci.*, 2022, **627**, 739–748.
68 K. Zhang, M. Dan, J. Yang, F. Wu, L. Wang, H. Tang and Z.-Q. Liu, *Adv. Funct. Mater.*, 2023, **33**, 2302964.
69 J. Hu, T. Yang, J. Chen, X. Yang, J. Qu and Y. Cai, *Chem. Eng. J.*, 2022, **430**, 133039.
70 L. Ye, K. Deng, F. Xu, L. Tian, T. Peng and L. Zan, *Phys. Chem. Chem. Phys.*, 2012, **14**, 82–85.
71 M. E. Aguirre, R. Zhou, A. J. Eugene, M. I. Guzman and M. A. Grela, *Appl. Catal., B*, 2017, **217**, 485–493.
72 P. Kumar, E. Vahidzadeh, U. K. Thakur, P. Kar, K. M. Alam, A. Goswami, N. Mahdi, K. Cui, G. M. Bernard, V. K. Michaelis and others, *J. Am. Chem. Soc.*, 2019, **141**, 5415–5436.
73 S. Yang, L. Li, W. Yuan and Z. Xia, *Dalton Trans.*, 2015, **44**, 6374–6383.
74 M. Arunachalapandi, T. Chellapandi, G. Madhumitha, R. Manjupriya, K. Aravindraj and S. M. Roopan, *Catalysts*, 2022, **12**, 1593.
75 S. Adhikari, A. V. Charanpahari and G. Madras, *ACS Omega*, 2017, **2**, 6926–6938.
76 S. Tharuman, V. Balakumar, J. Vinodhini, R. Karthikeyani, J. Mayandi, V. Sasirekha and J. M. Pearce, *J. Mol. Liq.*, 2023, **371**, 121101.
77 P. K. Sahu, R. Alaka, A. Champati, A. Madual, P. M. Mishra, A. Pradhan and N. Brundabana, *J. Met., Mater. Miner.*, 2025, **35**, e2241.